KeAi
CHINESE ROOTS
GLOBAL IMPACT

Available online at www.keaipublishing.com/en/journals/journal-of-magnesium-and-alloys/

ScienceDirect

Journal of Magnesium and Alloys 14 (2026) 101954

www.elsevier.com/locate/jma

Review

Atomic-scale modeling of defects in magnesium and its alloys: A review

Zhuocheng Xie[a,*], Julien Guénolé[b,*], Hexin Wang[a], Joé Petrazoller[b], Fatim-Zahra Mouhib[b], Antoine Guitton[b], Thiebaud Richeton[b], Stéphane Berbenni[b], Talal Al-Samman[a]

[a] *Institut für Metallkunde und Materialphysik, RWTH Aachen University, 52056 Aachen, Germany*
[b] *Université de Lorraine, CNRS, Arts et Métiers Institute of Technology, LEM3, F-57000 Metz, France*

Received 10 October 2025; received in revised form 26 October 2025; accepted 3 November 2025
Available online 11 December 2025

Abstract

Magnesium (Mg) and its alloys, known for their low density and high specific strength, are increasingly explored as lightweight structural materials across a broad range of industrial applications. However, their widespread application remains constrained by intrinsic mechanical limitations, fundamentally rooted in the nature of crystallographic defects. Atomic-scale modeling techniques are transforming our ability to unravel the structures, energetics, and dynamics of these defects and to explore their complex interactions, thereby guiding defect engineering in Mg alloys. However, the growing body of available data can make it difficult for researchers to identify critical knowledge gaps and promising areas for further exploration. To address this challenge, we highlight key research domains with significant potential for impactful advancements, aiming to illuminate these areas while inspiring innovative approaches and encouraging deeper exploration of pivotal topics that may shape the future of Mg alloy development. This review presents a comprehensive overview of the state-of-the-art in atomic-scale modeling of defects in Mg and its alloys. We introduce key simulation methodologies, including density functional theory and atomistic simulations, and highlight their applications to defect distribution, defect dynamics, and defect-defect interactions. By bridging fundamental insights in defects with alloy design strategies, this review aims to support and inspire the broader Mg research community and to underscore the growing impact of atomic-scale modeling in the accelerated development of high-performance Mg alloys.

Keywords: Magnesium; Atomistic simulations; Density functional theory; Crystallographic defects.

1. Introduction

Among structural metals, magnesium (Mg) alloys stand out due to their excellent strength-to-weight ratio. In recent years, they have received considerable attention for engineering applications focused on weight reduction, particularly in the automotive industry where minimizing mass is crucial [1,2]. In the race for greener and more efficient mobility, automakers turn to Mg alloys to lighten vehicle structures, boost fuel economy, and lower CO_2 emissions [3,4]. Aerospace engineers also capitalize on its high specific strength and natural vibration-damping properties to build quieter and lighter aircraft [5]. Furthermore, Mg alloys are also making strides into unexpected fields: shielding electronics from electromagnetic interference [6] and even serving as bioresorbable implants for bone healing [7]. From roadways to outer space and laboratories to operating theaters, Mg alloys are pioneering a new era of high-performance materials in strength and lightness.

While Mg alloys offer many benefits, their Achilles' heel remains their fundamental mechanical limitations. In particular, their inherently low ability to accommodate plastic strain during the processing of wrought products such as sheets and extrusions limits both ductility and formability. Additionally, the unidirectional nature for twinning activation in *c*-axis extension or contraction introduces a marked asymmetry between tensile and compressive responses, resulting in

Peer review under the responsibility of Chongqing University.
* Corresponding authors.
E-mail addresses: xie@imm.rwth-aachen.de (Z. Xie), julien.guenole@univ-lorraine.fr (J. Guénolé).

https://doi.org/10.1016/j.jma.2025.11.014

uneven yielding and work-hardening behavior [8–11]. These limitations are inherently tied to the hexagonal close-packed (HCP) crystal structure of Mg, which restricts the activation and stability of non-basal prismatic $\langle a \rangle$ and pyramidal $\langle c+a \rangle$ slip [12]. To accommodate plastic strain along the c-axis, Mg commonly activates deformation twinning, preferentially $\{10\bar{1}2\}$ extension twins, which reorients the crystal lattice by approximately 86°, leading to pronounced changes in crystallographic texture. The activation of twinning can either facilitate or hinder further deformation, depending on factors like grain orientation, processing route and loading conditions [13,14]. Twinning not only contributes to strain accommodation and ductility but can also act as a barrier to dislocation motion or promote crack initiation under certain circumstances [15]. In addition, grain boundaries (GBs) and second-phase precipitates influence plastic deformation by serving as obstacles for dislocation motion and twin propagation, as well as preferential sites for heterogeneous nucleation of defects [16]. Consequently, tailoring defect behavior through alloying and thermomechanical processing has therefore become a central focus to overcome the mechanical limitations of Mg alloys [17–22]. A comprehensive understanding of defect structures and dynamics, and their interactions with solute additions, is essential for developing effective strategies in the Mg-based materials design.

Fig. 1 illustrates a bottom-up design strategy for Mg alloys, where atomistic insights form the foundation for understand-

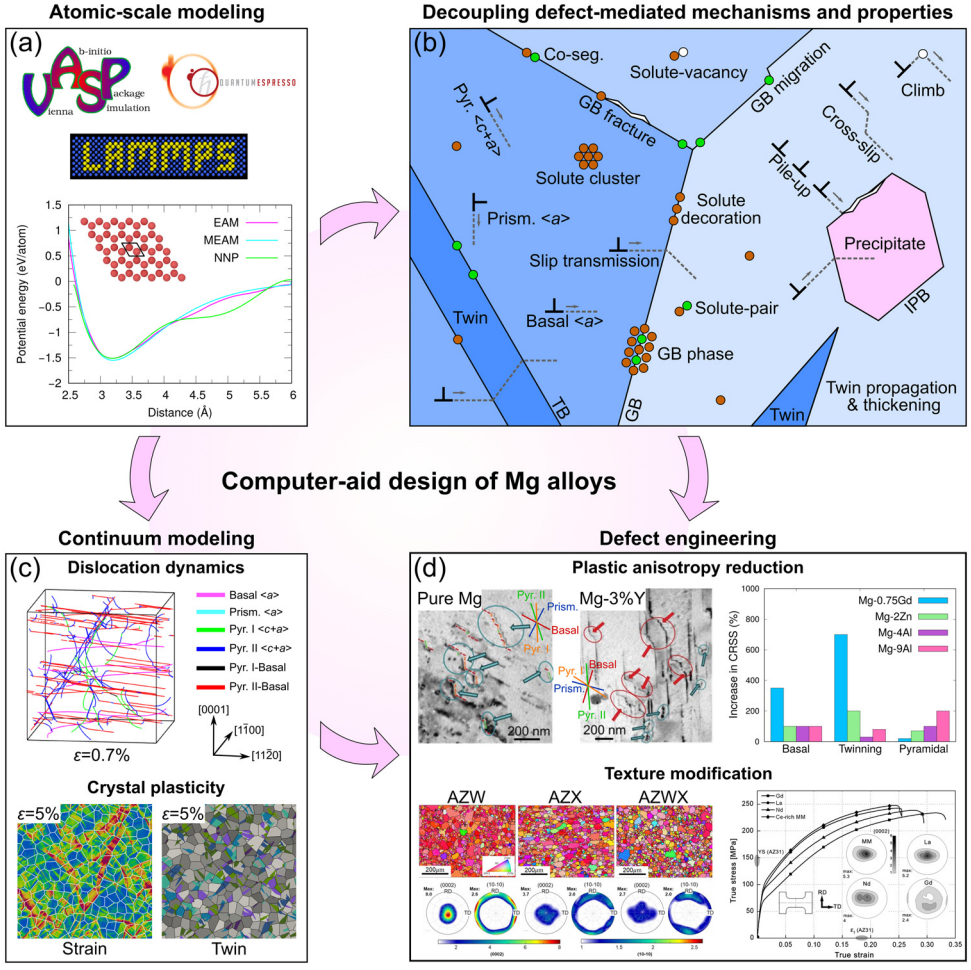

Fig. 1. Computer-aided design of Mg alloys use a bottom-up approach, from atomistic understanding to microstructural tailoring. (a) Atomic-scale modeling techniques, including ab-initio calculations [23,24] and atomistic simulations [25], have been extensively applied to Mg research. Semi-empirical interatomic potentials such as the embedded atom method (EAM) [26] and modified embedded atom method (MEAM) [27], and machine learning interatomic potentials (MLIP)[28] have been developed and widely used in atomistic simulations. (b) Atomic-scale modeling enables the decoupling of defect-mediated mechanisms and material properties in Mg and its alloys, by capturing the thermodynamics and kinetics of crystallographic defects from 0D to 3D (e.g., point defects, dislocations, GBs, precipitates) and defect-defect interactions. (c) Atomistically informed continuum modeling approaches, such as dislocation dynamics [29] and crystal plasticity simulations [30], have provided significant insights into the deformation behavior of Mg and its alloys. (d) Defect engineering strategies in Mg alloys, aimed at reducing plastic anisotropy and modifying texture, are increasingly informed by atomic-level insights. Top-left: Dislocation structures in pure Mg and Mg-3Y, showing enhanced stability of pyramidal dislocations in Mg-Y alloys [22]. Top-right: In Mg-0.75Gd, the activation of basal slip and twinning is notably suppressed compared to pure Mg and other Mg alloys [18–21]. Bottom-left: Texture modification achieved through Y additions in Mg alloys [20]. Bottom-right: Resulting improvement in mechanical properties due to RE-induced texture modification in Mg alloys [17]. Reprinted with permission from publishing houses.

ing defect-mediated mechanisms and their influence on material properties. Atomic-scale modeling plays a central role in decoupling the contributions of crystallographic defects ranging from 0-dimensional (0D) to 3D and in revealing how their behavior evolves with solute additions and thermodynamic variables, see Fig. 1(b). These atomistic insights also serve as essential input for mesoscale and continuum models that connect microstructural features to macroscopic mechanical responses, as illustrated in Fig. 1(c). Ultimately, this cross-scale computer-aided framework could support the design of Mg alloys with enhanced mechanical performance, such as weakened plastic anisotropy and controlled texture, through targeted defect engineering strategies (Fig. 1(d)).

In this review, we summarize recent progress in the atomic-scale modeling of defects in Mg and its alloys. We begin by introducing the widely used simulation techniques and their capabilities and limitations (Section 2). We then focus on major defect types in Mg and its alloys that are intrinsically linked to mechanical properties, including solute distributions (Section 3), dislocations (Section 4), twinning (Section 5), grain boundaries (Section 6), and dislocation-defect interactions (Section 7), emphasizing the underlying defect mechanisms and their implications for mechanical properties. Studies on free surfaces, which are critical to understanding oxidation and corrosion phenomena in Mg, are not covered here, as they are considered extrinsic to mechanical properties within the scope of this review. Finally, we conclude with perspectives on future challenges and opportunities in this rapidly evolving field (Section 8). We hope this review will inform and inspire the broader Mg research community by showcasing the expanding role and potential of atomic-scale modeling in driving both fundamental understanding and alloy design.

2. Atomic-scale modeling techniques

Atomic-scale modeling techniques have become indispensable for understanding the fundamental mechanisms that govern material behavior at the atomic level. In recent years, these techniques have enabled in-depth investigations into the structures, energetics, and dynamics of crystallographic defects from 0D to 3D, which critically influence the macroscopic properties of Mg and its alloys. In this section, we provide a brief introduction to the most widely used atomic-scale simulation approaches, focusing on their capabilities, applications, and limitations in defect studies of Mg-based systems. For readers seeking a more comprehensive introduction to atomic-scale modeling techniques, several excellent textbooks are recommended [31–34].

2.1. Density functional theory

Density functional theory (DFT) is a quantum mechanical method that provides highly accurate predictions of material properties by solving the electronic structure of atoms and their interactions. In the context of Mg and its alloys, DFT has played a central role in calculating both fundamental bulk properties, such as lattice constants and elastic moduli, and defect properties, including stacking fault energies (SFEs), dislocation core structures, GB structures and energies, and solute segregation energies. However, due to its high computational cost, which scales approximately as $\mathcal{O}(N^3)$, DFT calculations are typically limited to systems containing only a few hundred atoms and are often applied under static (zero-temperature) conditions. As a result, its application is generally restricted to modeling highly symmetric defects in Mg, such as specific coincidence site lattice (CSL) GBs [35,36] and twin boundaries (TBs) [37,38]. Another challenge arises in the treatment of rare-earth (RE) elements in DFT, which are widely used alloying elements in Mg alloys. RE elements are typically modeled using pseudo-potentials that treat the highly localized $4f$ electrons as part of the atomic core, referred to as the "frozen $4f$" approximation [39,40]. While this approach significantly reduces computational complexity, it may compromise the accuracy in describing chemical bonding involving RE elements. Despite these constraints, DFT remains the most reliable method for capturing energetics and electronic effects, and the results can also serve as a critical reference for developing and validating semi-empirical and machine-learned interatomic potentials used in larger-scale atomistic simulations.

2.2. Classical atomistic simulations

Classical atomistic simulations provide a powerful and computationally efficient means of studying large systems (up to millions of atoms) and accessing dynamic processes at finite temperatures over timescales ranging from picoseconds to microseconds. These simulations rely on predefined interatomic potentials or force fields that approximate the interatomic interactions based on semi-empirical or machine-learned functional forms. This approximation significantly reduces the computational cost, allowing simulations to scale linearly with the number of atoms ($\mathcal{O}(N)$). These capabilities make classical atomistic simulations an essential tool for bridging atomic-scale mechanisms to experimentally observed defect phenomena in Mg and its alloys.

2.2.1. Interatomic potentials

Interatomic potentials are at the core of atomistic simulations, as they define how atoms interact based on simplified representations of quantum mechanical forces. Their accuracy directly determines the reliability of simulations in predicting defect structures and energetics at the atomic scale. For Mg and its alloys, a variety of interatomic potentials have been developed to capture key bulk and defect properties. These potentials vary in complexity, from classical physics-inspired empirical forms to modern machine learning-based approaches. For a broader overview of interatomic potentials, the reader is referred to several comprehensive review papers [52–54].

- **Embedded atom method (EAM)**[55] is one of the most widely used empirical potential frameworks for metallic

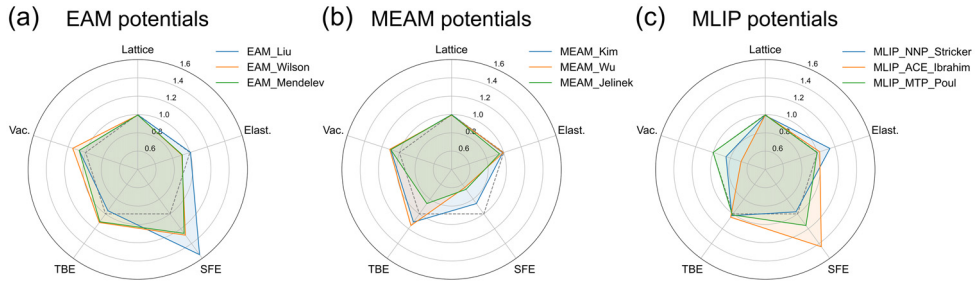

Fig. 2. Radar plots showing the performance of various Mg interatomic potentials across five basic material properties: lattice parameters (Lattice), elastic constants (Elast.), basal I1 and I2 stacking fault energies (SFE), tensile and compression twin boundary energies (TBE), and vacancy formation energy (Vac.). Each property is normalized against corresponding experimental [41,42] or DFT [43,44] reference values, with a value of 1.0 indicating perfect agreement. The dashed grey pentagon denotes the ideal reference level. Three categories of potentials are compared: (a) EAM [26,45,46], (b) MEAM [27,47,48], and (c) MLIP [49–51]. The closer the shape is to the reference pentagon (grey dashed), the better the overall predictive accuracy of the potential.

systems. It models atomic interactions by combining pairwise interactions with an embedding energy that mimics the effect of the local electron density. EAM potentials offer a good compromise between computational efficiency and accuracy for modeling bulk and defect properties in metals like Mg. However, their limited flexibility can lead to reduced accuracy when dealing with complex or low-symmetry crystalline and defect configurations, such as the bulk properties of Mg-based intermetallics [56] and the core structures and dynamics of pyramidal dislocations in Mg [57].

- **Modified embedded atom method (MEAM)**[58] is an extension of the EAM formalism by incorporating angular dependencies into the interaction terms. This enhancement allows MEAM to better capture directional bonding and more complex atomic environments, which are especially important in Mg and its alloys. The incorporation of angular terms also increases computational complexity, making MEAM roughly an order of magnitude more expensive than EAM potentials. The added complexity improves the potential's transferability across different crystal structures and defect types, making it particularly well-suited for simulations involving dislocations, GBs, and precipitates in Mg-based systems.
- **Machine learning interatomic potentials (MLIPs)** use data-driven models trained on DFT calculations to predict interatomic forces and energies. Common MLIP frameworks include neural network potentials (MLIP_NNP) [59], atomic cluster expansion (MLIP_ACE)[60] potentials, and moment tensor potentials (MLIP_MTP) [61]. These models can achieve near-DFT accuracy while being significantly faster than first-principles methods, making them powerful tools for simulating structurally and chemically complex systems with high fidelity. However, their reliability is highly dependent on the quality and representativeness of the training dataset. Additionally, despite substantial speed-ups over DFT, MLIPs remain orders of magnitude more computationally demanding than classical semi-empirical potentials, which can limit their practical use in simulations involving large numbers of atoms and/or time scales.

Selecting an appropriate interatomic potential is crucial for ensuring the reliability of atomistic simulations and should be guided by the specific research questions and the critical material properties of interest. Different potentials vary in their ability to reproduce key physical quantities. Therefore, it is essential to choose a potential that has been validated against the relevant properties for the system and phenomena under investigation. Fig. 2 provides a comparative overview of several widely used Mg potentials, illustrating their performance across a set of benchmark properties relative to experimental and DFT reference values. The benchmarking methodology and reference data are described in detail in Wang et al [57]. All interatomic potentials benchmarked in this work exhibit good accuracy in predicting lattice parameters and elastic constants, indicating that elastic deformation behaviors, including the pronounced elastic anisotropy of Mg, can be well captured by these models. However, noticeable differences arise in the prediction of SFEs. Specifically, all EAM potentials tend to overestimate the basal SFEs (I1 and I2), whereas all MEAM-type potentials underestimate them, particularly MEAM_Wu and MEAM_Jelinek. Among the MLIPs, MLIP_NNP_Stricker shows the best agreement with ab-initio reference data, followed by MLIP_MTP_Poul. The I2 basal SFE directly affects the dissociation width of basal dislocations and consequently the corresponding Peierls stress. A more detailed discussion of the performance of these potentials, particularly the limitations of EAM potentials in modeling non-basal dislocations, such as unstable pyramidal configurations and artificial intermediate states in prismatic dislocations, is provided in Section 4. For twin boundary (TB) formation energies ($\{10\bar{1}1\}$ and $\{10\bar{1}2\}$ TBs), all tested potentials show reasonable agreement with ab-initio data, with MLIPs performing particularly well. The semi-empirical potentials also demonstrate consistent trends in predicting the variation of formation energies as a function of the misorientation angle of $\langle c\rangle$-axis tilt GBs [57]. This suggests that semi-empirical potentials could be applied to effectively reduce the parameter space of microscopic degrees of freedom in GB studies, before applying more accurate MLIPs for detailed investigations of specific boundaries. In contrast to their generally good performance in other material properties,

Table 1
Comparison of commonly used interatomic potentials for Mg and its alloys, summarizing their key characteristics and recommended application domains in atomic-scale modeling of defects.

Potential	Key characteristics	Recommended application domains
EAM	Well-established for metallic bonding; computationally efficient	Basal dislocation motion; twinning; GB structures and energies; initial screening of defect configurations
MEAM	Incorporating angular dependence to better capture directional bonding; moderate accuracy at relatively low computational expense	Non-basal dislocation motion; dislocation cross-slip; GB motion; solute effects on defect dynamics; defect-precipitate interactions; nanomechanical testing
MLIP	Data-driven potentials trained on ab-initio datasets; provide near-ab-initio accuracy but high computational cost	Solute clustering; dislocation cores; slip mechanisms; interphase boundaries; solute-defect interactions; metastable defect phases; validation of semi-empirical potentials

most MLIPs, except MLIP_MTP_Poul, exhibit limited accuracy in predicting vacancy formation energies compared with semi-empirical potentials. This indicates that caution should be exercised when applying these MLIPs to model vacancy-related processes, such as vacancy diffusion and dislocation climb. Incorporating more vacancy-related ab-initio reference data into MLIP training datasets would likely improve their transferability and predictive reliability for vacancy diffusion phenomena. Overall, MLIP_MTP_Poul demonstrates the most balanced and reliable performance across the various properties examined in this work.

While the benchmarking results highlight the varying levels of accuracy among different interatomic potentials, it is equally important to consider their practical trade-offs and suitability for specific simulation tasks. The marginal gains in accuracy offered by MLIPs are often most justified in studies where precise defect energetics and structures are critical, such as investigations of dislocation core or solute clustering and segregation. In contrast, well-validated MEAM or EAM potentials remain preferable for large-scale atomistic simulations where computational efficiency is essential, for instance, in modeling defect dynamics, defect-defect interactions, or nanomechanical testing involving millions of atoms. The choice of potential should therefore balance fidelity and efficiency according to the targeted phenomena and relevant length- and time-scales. To aid this selection, Table 1 summarizes the recommended application domains and key strengths of EAM, MEAM, and MLIP potentials. This comparative perspective underscores that no single potential universally outperforms others; rather, each serves best within its optimal regime defined by the physical complexity, accuracy requirements, and computational constraints of the problem under study.

2.2.2. Molecular statics

Molecular statics (MS) is a computational approach that determines the minimum energy configuration of a system by relaxing atomic positions, without accounting for time evolution or physical atomic trajectories. By minimizing the system's potential energy, e.g., using damping algorithms [62], MS enables the identification of stable or metastable atomic structures, including various crystallographic defects, under specified boundary or loading conditions. It is particularly well-suited for quantifying binding energies, defect formation energies, and solute segregation energies.

In addition to static relaxation, quasi-static simulations offer a useful extension of MS for exploring the mechanical response of materials under incremental loading. In this approach, the system is gradually deformed in small steps, with energy minimization performed after each increment to trace the equilibrium deformation path. This method is particularly useful for calculating the Peierls stress, namely the critical resolved shear stress required to move a dislocation at zero temperature. By incrementally applying shear and relaxing the system after each step, the onset of dislocation motion can be identified [63]. Quasi-static simulations have been widely used to study defect mobility and mechanical thresholds under athermal conditions.

Another powerful extension of MS is the nudged elastic band (NEB) [64,65] method, which is used to determine the minimum energy path and associated activation barriers for atomic-scale transition events, such as dislocation glide, cross-slip, or point defect migration. NEB works by interpolating a series of intermediate images between initial and final atomic configurations and iteratively optimizing them to map the most energetically favorable transition pathway. The resulting energy barrier, when combined with transition state theory (TST), provides insights into the thermally activated nature of defect evolution, facilitating connections between atomistic mechanisms and macroscopic deformation behavior.

Although molecular statics cannot capture dynamic or temperature-dependent behavior, it remains an efficient and widely used method for determining ground-state defect structures and formation energies, especially when anharmonic effects are minor compared to the overall structural stability.

2.2.3. Molecular dynamics

Molecular dynamics (MD) simulations track the time evolution of atomic systems by solving Newton's equations of motion, providing a dynamic view of defect nucleation, evolution, and interaction at finite temperatures. MD allows for the direct observation of dynamic processes such as solute diffusion, dislocation glide, twinning, GB migration, and phase transformations, which are particularly valuable

for studying temperature and rate-dependent phenomena and critical for understanding material behavior in Mg and its alloys.

However, MD simulations are inherently constrained by accessible time and length scales, typically covering tens to hundreds of nanoseconds and system sizes up to few hundred nanometers. These constraints arise from the need for extremely small time steps to accurately resolve atomic vibrations governed by the characteristic phonon frequencies (on the order of femtoseconds), as well as the computational cost associated with large-scale massively parallel simulations. As a result, many processes that occur over microseconds or above micrometers in experiments are challenging to model directly. Despite these limitations, MD remains a powerful and widely used tool for investigating atomic-scale mechanisms. Its impact is further enhanced when coupled with other simulation techniques, such as ab initio calculations for improving accuracy, Monte Carlo methods for extending time scales, and continuum-scale simulations for bridging to larger length scales, enabling a more comprehensive understanding of defect behavior in Mg and its alloys.

2.3. Monte Carlo

Monte Carlo (MC) is a stochastic sampling technique to explore the configurational space of atomic systems and is particularly effective for modeling thermodynamics within the framework of statistical mechanics. MC methods are grounded in the minimization of the Gibbs free energy, where configurational sampling allows the system to explore a broad ensemble of atomic arrangements. The stochastic sampling inherent in MC effectively captures the configurational entropy, which is crucial in determining phase stability at finite temperatures. By efficiently sampling thermodynamically relevant configurations, MC methods provide direct access to equilibrium states without explicitly resolving kinetic pathways. Therefore, they are particularly valuable in scenarios where thermodynamic equilibrium states under varying chemical potentials are the primary focus, and where kinetic barriers are not of interest.

In Mg alloys, MC simulations are widely applied to investigate solute distributions in equilibrium, such as solute segregation, short-range chemical ordering, and the formation of Guinier–Preston (GP) zones or ordered intermetallic phases. These insights are critical for understanding and predicting phase stability and the thermodynamic driving forces behind microstructural evolution.

2.4. Hybrid techniques

To overcome the time scale limitations of classical MD and improve the accuracy of atomistic simulations, hybrid atomic-scale techniques integrate the strengths of different computational approaches, such as quantum mechanical accuracy, classical simulation efficiency, and enhanced sampling methods, into unified frameworks. These multiscale and hybrid strategies allow us to capture defect phenomena that are inaccessible to any single technique.

2.4.1. Quantum mechanics/molecular mechanics

Quantum mechanics/molecular mechanics (QM/MM)[66] is a multiscale simulation method that combines the accuracy of quantum mechanical (QM) calculations with the efficiency of classical molecular mechanics (MM) simulations. In this approach, a small region of interest, typically where energetic accuracy is essential, such as solute occupation sites, dislocation cores, or crack tips, is treated using DFT, while the surrounding environment is modeled using a classical interatomic potential. The QM and MM regions are coupled through boundary conditions that ensure consistency of atomic forces and energies across the interface. QM/MM offers a practical framework for exploring complex and sensitive phenomena where fully quantum mechanical treatments are computationally prohibitive. QM/MM has been employed to investigate solute segregation at crystallographic defects in metals, which allows for accurately capturing the chemical specificity and local bonding environments of solute atoms, while still considering their interaction with extended defect structures [67,68].

2.4.2. Hybrid MC/MD

Hybrid MC/MD methods couple the strength of both configurational sampling and lattice dynamics to more effectively simulate chemically complex systems. In hybrid MC/MD schemes, MC steps, involving atom-type exchanges, are interleaved with MD runs that evolve the system at finite temperatures. The semi-grand canonical (SGC) and variance-constrained semi-grand canonical (vc-SGC) ensembles are the most widely used schemes [69]. The SGC ensemble fixes the chemical potential difference between species, permitting atom transmutations that mimic chemical fluctuations and phase separation under constrained average composition. The vc-SGC ensemble, introduced to address challenges in convergence and control of local composition, imposes an additional constraint on compositional variance. This modification stabilizes fluctuations and improves sampling efficiency, particularly important in systems exhibiting strong phase separation tendencies or near miscibility gaps.

In Mg alloys, hybrid MC/MD simulations have been applied to study temperature- and concentration-dependent solute clustering, solute segregation, and defect precipitation [71,72]. These methods provide a powerful framework for exploring the solute enrichment landscape of Mg alloys as a function of chemical potential, offering valuable insights into thermodynamic driving forces behind structural transformation in compositionally inhomogeneous systems.

2.5. Structural characterization

Analyzing atomic configurations generated by simulations requires robust structural characterization methods, particu-

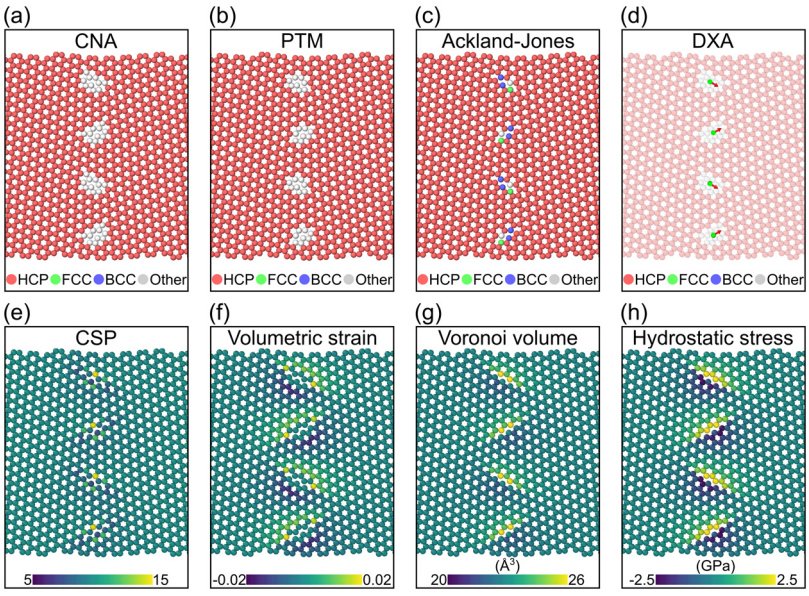

Fig. 3. Structural characterization methods applied on a Σ31 ⟨0001⟩ symmetric tilt GB (STGB) ($\theta = 50.57^{\circ}$) in Mg: (a) Common neighbor analysis (CNA); (b) polyhedral template matching (PTM); (c) Ackland-Jones analysis; (d) dislocation extraction algorithm (DXA), with dislocation lines colored in green, Burgers vectors illustrated as red arrows, and atoms rendered half-transparent; (e) centrosymmetry parameter (CSP); (f) elastic volumetric strain; (g) Voronoi volume; (h) hydrostatic virial stress. The simulation methodology and reference data are described in detail in Zhang et al [70].

larly for the accurate identification and characterization of crystallographic defects, such as dislocations, stacking faults, GBs, and secondary phases, in Mg and its alloys. Structural analysis of these defects is essential for understanding their thermodynamic stability and kinetic behavior, and for establishing meaningful correlations between atomic-scale modeling and experimentally observed phenomena. Several commonly used tools include:

- **Common neighbor analysis (CNA)**[73] is a geometry-based method that classifies local atomic environments by evaluating the bonding patterns of neighboring atoms, distinguishing structures such as face-centered cubic (FCC), HCP, and body-centered cubic (BCC).
- **Polyhedral template matching (PTM)**[74] is a structural analysis algorithm that compares local atomic arrangements to ideal templates, offering improved robustness to thermal vibrations and rotational invariance.
- **Ackland-Jones analysis**[75] is a method for identifying common crystalline and other structures based on an analysis of the distribution of angles formed by the pairs of neighbors of a central atom.
- **Dislocation extraction algorithm (DXA)**[76] is a computational method that identifies and characterizes dislocation lines, including their Burgers vectors and line directions, directly from atomic positions.
- **Centrosymmetry parameter (CSP)**[77] is a measure of the local lattice disorder around an atom and can be used to characterize whether the atom is part of a perfect lattice or a local defect.
- **Elastic strain**[78] computes the atomic-level elastic deformation gradient tensors, which map ideal lattice vectors to the actual distorted configuration, allowing analysis of local elastic strain and crystal orientation without needing a reference snapshot.
- **Voronoi volume**[79] refers to the space around an atom that is closer to that atom than to any other, forming a unique polyhedral cell for each atom in a structure, also known as Wigner–Seitz cell. It provides a way to estimate the local atomic volume and can be used to analyze packing efficiency, local density, or detect structural defects.
- **Virial stress**[80] is a measure of stress on an atomic scale, computed from the forces and positions of atoms.
- **Laves phase Crystal Analysis (LaCA)**[81] is a structural analysis algorithm tailored for identifying intermetallic phases, such as Laves phases, by comparing local atomic motifs to known crystal structures.

The performance of these tools in the identification of crystallographic defects in Mg, i.e., dislocations and GBs, is illustrated in Fig. 3. CSP, elastic strain, Voronoi volume, and virial stress describe the local atomic configuration by assigning per-atom values, with defect structures revealed through color mapping or by subtracting differences from the matrix properties (see Fig. 3(e-h)). In contrast, CNA and PTM require predefined parameters but classify atoms into specific crystal structures (HCP, FCC, or BCC). Compared with CNA and PTM, the Ackland–Jones analysis is generally considered less robust, particularly when applied to strongly distorted crystal structures. These tools help bridge atomistic results with experimental observations, such as those from atomic-resolution scanning transmission electron microscopy (STEM) or atom probe tomography (APT).

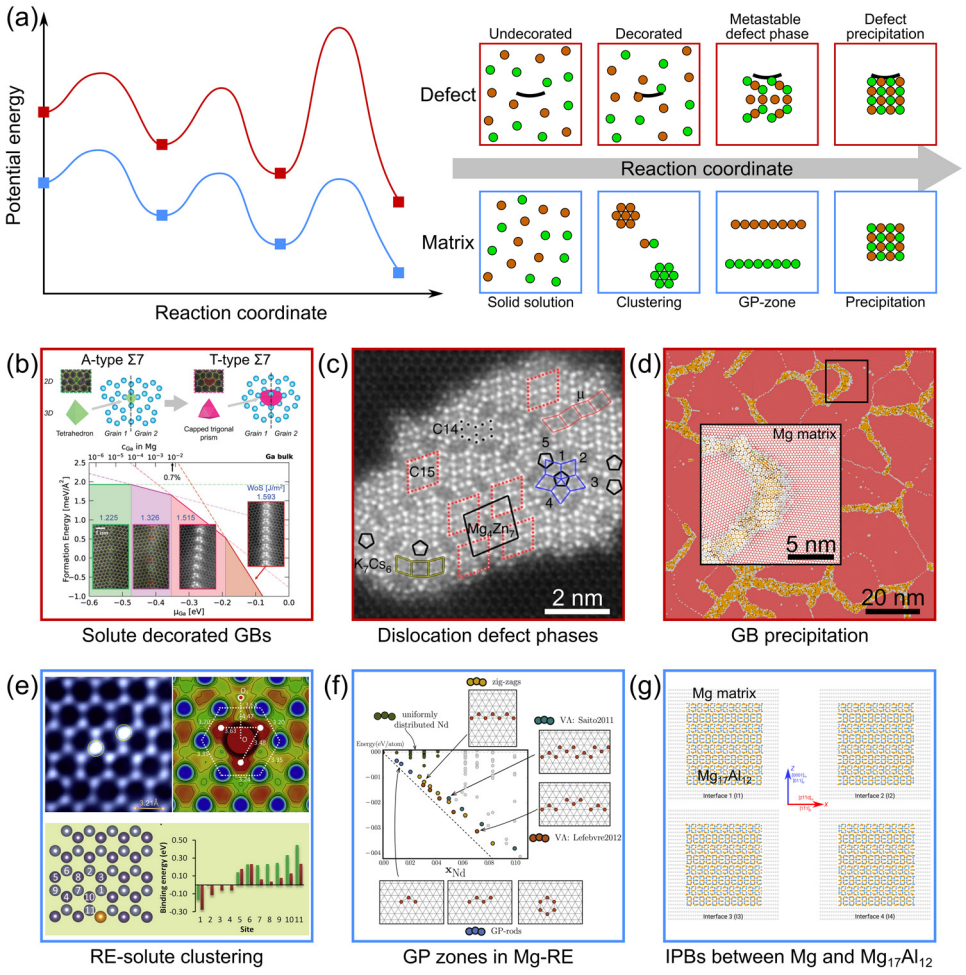

Fig. 4. Solute distribution in bulk Mg and around crystallographic defects. (a) Schematic illustration of the solute segregation landscape, showing the progression from undecorated defects to solute-decorated defects, followed by the formation of metastable defect phases [82], and ultimately defect-associated precipitation. In the matrix, solute behavior transitions from a random solid solution to solute clustering, then to the formation of Guinier–Preston (GP) zones, and finally to bulk precipitation. (b) Structural transformation of Σ7 GBs from the A-type structural unit to the T-type structural unit in Mg alloys with increasing Ga content [36]. The accompanying defect phase diagram summarizes both experimentally observed GB structures and corresponding energies calculated using DFT. (c) Formation of dislocation defect phases in a Mg–Zn alloy, including topologically close-packed (TCP) phases and other structurally complex crystals associated with an ⟨*a*⟩ dislocation [83]. (d) GB precipitation in Mg alloys as revealed by atomistic simulations [71]. (e) Isolated solute cluster containing two Nd atoms in Mg, with electron charge density calculated using DFT [84]. Structural models illustrate substitutional incorporation of two columns of solute atoms in the Mg lattice, along with their corresponding binding energies. (f) Formation energies of various GP zones in Mg–Nd alloys as calculated using DFT [85]. (g) Atomistic modeling of interphase boundaries (IPBs) between the Mg matrix and the $Mg_{17}Al_{12}$ precipitate [86]. Reprinted with permission from publishing houses.

3. Solute distribution

3.1. Solute enrichment landscape

The spatial distribution of solutes in HCP Mg plays a crucial role in determining thermodynamic stability and plastic response. It is governed by solute type, concentration, and thermodynamic variables, thus offering key levers for tailoring strength, ductility, and thermal stability of Mg alloys. Fig. 4(a) schematically illustrates solute enrichment pathways in the bulk matrix and at crystallographic defects. Within the matrix, solute enrichment evolves through a sequence of stages beginning with a random solid solution, proceeding to solute clustering and short-range order (SRO), advancing to formation of GP zones and metastable intermediate precipitates, and culminating in equilibrium (bulk) precipitation. Each successive stage imparts distinct contributions to the macroscopic behavior. Solid-solution strengthening arises from local lattice distortions induced by elastic misfit between solute and solvent atoms, which hinder dislocation motion. The formation of atomic clusters and precipitates introduces coherent or semi-coherent obstacles within the matrix. Depending on their size, spacing, and interfacial structure, they may be sheared by dislocations or bypassed via Orowan looping, thereby tuning yield strength, work hardening, and strain-rate sensitivity [16]. Meanwhile, co-clustering and SRO can significantly affect stacking-fault energies and dislocation core structures, shifting the relative

ease of basal versus non-basal slip and influencing twinning propensity [87].

Beyond the matrix, crystallographic defects serve as low-energy sinks for solute segregation. As shown in Fig. 4(a), segregation often initiates by solute decoration of dislocations, TBs and GBs. With increasing chemical driving forces, localized solute accumulation at defects can trigger structural transformations to metastable defect phases with distinct chemical and structural configurations from the matrix [82]. These phases may be kinetically stabilized by substantial energy barriers before eventually evolving into thermodynamically stable precipitates anchored at defects. Such localized chemical enrichments and structural transformations can profoundly alter defect-mediated plasticity, GB mobility, and interfacial cohesion. Through these mechanisms, solute–defect interactions offer powerful means for tuning material properties. Accordingly, a mechanistic understanding of the energetics, kinetics, and pathways of solute segregation and their subsequent impact on defect properties remains central to modern defect engineering and the design of high-performance Mg-based materials.

This section focuses on atomic-scale modeling of solute enrichment within the matrix, covering solute binding, diffusion, clustering, and precipitation. In Sections 4, 5, and 6, we extend this discussion to solute segregation at various crystallographic defects in greater detail.

3.2. Solute binding

Recent advances in atomic-scale modeling have shed light on the fundamental thermodynamics and kinetics underlying solute distribution in Mg alloys. Solute–solute binding energies have been systematically evaluated using DFT across a broad range of binary and ternary Mg alloys, providing a thermodynamic basis for understanding clustering tendencies and SRO phenomena [88,89]. Similarly, solute–vacancy binding energies, particularly those involving RE elements, have been calculated using DFT [90,91]. Saal and Wolverton [90] reported that light RE elements (La to Gd) exhibit favorable vacancy binding, while heavier RE elements (Tb to Lu) show weaker or even repulsive interactions. A strong linear correlation between binding energy and solute-induced lattice relaxation highlighted the role of strain energy minimization in driving solute segregation. More recently, Mouhib et al. [92] compared solute–vacancy and solute–solute binding in Mg–Ca–(Zn) and Mg–Gd–(Zn) systems, finding that Ca binds more strongly with vacancies than Gd, while Zn exhibits stronger co-segregation with Gd than with Ca. These computational findings align with APT observations on solute distribution and offer a mechanistic explanation for observed segregation patterns and their influence on texture evolution in Mg alloys.

3.3. Solute diffusion

The diffusion characteristics of solutes in Mg have been extensively investigated through atomic-scale modeling techniques. Migration barriers of solutes in the Mg matrix have been calculated using DFT [93,94]. Zhou et al. [94] estimated diffusion coefficients through TST, showing that transition metals typically display strong vacancy binding and high diffusion barriers. Agarwal and Trinkle [95,96] developed a Green's function model for vacancy-mediated solute diffusion in Mg, incorporating DFT-based energetics. Using a self-learning kinetic Monte Carlo (KMC) method, Nandipati et al. [97] simulated Al diffusion in Mg using on-the-fly barrier calculations, uncovering anisotropic diffusion behavior, with faster transport occurring along the basal plane. Yi et al. [72] studied solute interactions with vacancy clusters using hybrid MD/MC simulations based on the MEAM_Kim potential, finding that solutes accelerate mono-vacancy diffusion while suppressing cluster mobility, thereby stabilizing clusters and promoting segregation, a trend validated by APT of aged Mg–Al alloys.

3.4. Early-stage precipitation

Solute clustering and GP zone formation in Mg alloys have been a central focus of recent atomic-scale modeling efforts. Nie et al. [84] combined atomic-resolution STEM with DFT to investigate clustering in Mg–Nd and Mg–Y alloys, revealing solute-enriched monolayer clusters aligned on the basal plane (Fig. 4e). These configurations were shown to minimize elastic strain energy, explaining their stability and uniform spacing. Kimizuka and Ogata [98] employed a multibody potential parameterized by DFT data to predict solute short-range ordering in Mg–Al–Gd alloys, identifying energetically favorable stacking fault-associated structures resembling long-period stacking order (LPSO) motifs. Saal and Wolverton [99] evaluated the thermodynamic stability of LPSO structures in Mg–Y–Zn alloys using DFT, showing that while these LPSO structures have negative formation energies, they are metastable relative to the ground-state phase diagram, suggesting their stability is kinetic rather than thermodynamic.

Natarajan et al. [85] combined DFT and MC simulations to model GP zone formation in Mg-Nd alloys, see Fig. 4(f). They proposed a hierarchy of hybrid phases (β'''') that evolve during early decomposition. Contrary to earlier assumptions, their results indicate that $D0_{19}$-like orderings are better described as disordered GP rods, reshaping the understanding of initial solute clustering. In follow-up work, Natarajan and Van der Ven [100] employed high-throughput DFT calculations to study the thermodynamic stability of hierarchical β''' phases in Mg–RE binary systems. They revealed that RE atoms can form either zigzag or hexagonal arrangements depending on the element, with these configurations influencing misfit strains and precipitate morphology, offering key insights for alloy design. Further, Natarajan and Van der Ven [101] utilized DFT combined with cluster expansion and MC simulations to investigate the phase stability of HCP, BCC, and FCC-based solute orderings in Mg-Sc alloys. Their work uncovered a diverse set of ordered and disordered phases, with Sc solutes forming rod-like and hierarchical motifs, and highlighted the role of phase competition in driving martensitic transformations. More recently, Cheng et al. [102] used DFT combined with cluster expansion methods to predict the

atomic configurations of ordered monolayer GP zones in Mg–Zn–X (X=Ca, Nd) systems, discovering metastable GP zone structures composed of Mg_2X motifs with partial Zn substitution, which agreed well with prior experimental data.

Atomistic simulations have complemented DFT by enabling finite-temperature and larger-length-scale insights. Jiang et al. [103] used KMC based on EAM potentials to investigate early-stage precipitation in Mg–RE alloys, showing that Y atoms preferentially aggregate along the *c*-axis, evolving from isolated clusters into six-membered rings and zigzag GP zones, consistent with STEM observations. Liao et al. [104] applied KMC simulations with an "on-lattice" interatomic potential for the Mg–Y–vacancy system based on their DFT to study the nucleation kinetics of β'' precipitates in Mg–Y alloys. They found an optimal nucleation temperature of 550 K and characterized the early-stage formation of solute clusters with zigzag and hexagonal motifs.

3.5. Precipitation

Intermediate metastable precipitates (β' and β_1) in Mg-based alloys, particularly Mg-RE binary and ternary alloys, have been investigated via DFT, with a focus on their formation energies, thermodynamic stability, morphologies, and interphase boundaries [105–118]. Issa et al. [119] investigated the stability and elastic properties of metastable Mg_3RE ($D0_{19}$) precipitates, finding that coherency strain energy favors prismatic over basal habit planes across all Mg–RE systems, thereby explaining the experimentally observed plate-like precipitate morphology. Later, Issa et al. [120] explored the Mg/β'' interface and revealed its energetic instability, which promotes transformation to the more stable β' phase, suggesting that β'' may act as a transient precursor during aging. Shi et al. [121] combined APT and DFT calculations to investigate Ca partitioning in Mg–Nd–Y alloys. Their results show that Ca can substitute for RE atoms in both β''' and β' precipitates without altering the precipitation sequence, offering a cost-effective strategy to reduce rare-earth usage. Hua et al. [122] combined multi-scale characterization with MD and MC simulations to reveal that atomic-scale Ca–Ce cocoon-like interfacial segregation in a dilute Mg–Mn–Al–Ca–Ce alloy stabilizes β-Mn nanoprecipitates by strain-driven solute redistribution and interfacial energy reduction, ensuring exceptional thermal stability.

Atomistic simulations have further advanced the understanding of precipitation behavior at larger scales. Atomistic simulations have revealed chemically and structurally complex interfacial regions that mediate lattice coherency and influence interface strength, as demonstrated in the $Mg/Mg_{17}Al_{12}$ (Fig. 4(g)) [86,123] and $Mg/CaMg_2$[124] systems. Additional insights into dislocation-precipitation interactions are reviewed in Section 7.

4. Dislocations

The HCP crystal structure of Mg inherently restricts the number of independent easy slip systems, leading to pronounced plastic anisotropy and limited ductility at room temperature. Dislocation activity in Mg predominantly occurs on three slip systems: basal $\langle a \rangle$, prismatic $\langle a \rangle$, and pyramidal $\langle c + a \rangle$ (see Fig. 5(a)). Among these, $\langle a \rangle$ dislocations on the basal plane facilitate easy slip and dominate deformation under most loading conditions. In contrast, $\langle c + a \rangle$ dislocations, gliding on pyramidal planes, are more difficult to activate but are essential for accommodating strain along the *c*-axis, thereby enabling true three-dimensional plasticity.

Atomic-scale modeling has been indispensable for elucidating the core structures, energetics, and motion mechanisms of dislocations in Mg and its alloys. Numerous studies have examined the stability and mobility of dislocations across different slip systems, often within the theoretical framework of the generalized stacking fault energy (GSFE). The GSFE surface characterizes the potential energy surface associated with rigid-body displacements along specific crystallographic planes, providing critical input for identifying favorable slip systems, possible dissociation pathways, and for estimating Peierls stresses via the Peierls–Nabarro model.

Recent work has moved beyond static characterizations to probe the dynamics of dislocation motion. Techniques such as NEB calculations and MD simulations have been employed to determine minimum energy paths and activation barriers, revealing rate-limiting steps and competing slip mechanisms. These atomistic insights provide a foundation for interpreting experimental observations and for designing alloying strategies that promote more isotropic plasticity and enhanced ductility in Mg alloys. For a broader introduction to atomic-scale modeling of dislocations, the reader is referred to several comprehensive textbooks and review articles [63,125].

4.1. Basal and prismatic $\langle a \rangle$ dislocations

Basal slip, involving dislocations with Burgers vectors of $\langle a \rangle$ on the (0001) plane, is the dominant deformation mode in Mg at room temperature. Prismatic $\langle a \rangle$ slip, while less frequently activated, can also accommodate strain, particularly under specific crystallographic orientations and loading conditions. Yasi et al. [126] and Shin and Carter [130] investigated core structures of basal and prismatic $\langle a \rangle$ dislocations in Mg using both ab initio methods and empirical EAM potentials [26,45]. While EAM potentials reproduce basal dislocation properties and SFEs reasonably well (see Fig. 5(b)), they tend to introduce artifacts when modeling non-basal dislocations. Shin and Carter [131] extended their DFT calculations to quantify Peierls stress of dislocations in Mg, revealing low Peierls stress for basal edge dislocation (0.6 MPa) and much higher stress for prismatic one (35.4 MPa). They attributed these differences to the presence or absence of stable stacking faults and the collective atomic motion within dislocation cores, achieving good agreement with experimental data. Qiu et al. [132] calculated the stress-dependent core structures of basal dislocations in Mg using DFT, finding that the Peierls stress for basal dislocations can vary by an order of magnitude depending on the applied stress, demonstrating pronounced non-Schmid effects in Mg crystal plasticity. More recently,

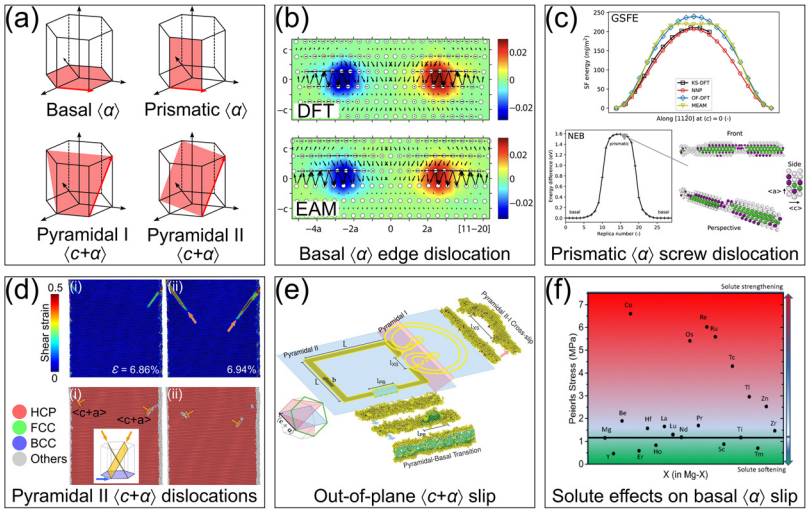

Fig. 5. Dislocation mechanisms in Mg and its alloys. (a) Schematic of the predominant slip systems: basal $\langle a \rangle$, prismatic $\langle a \rangle$, and pyramidal I and II $\langle c+a \rangle$. (b) Core structure of a basal $\langle a \rangle$ edge dislocation modeled using DFT and the EAM_Mendelev potential [126], with differential displacement vectors and the Nye tensor color map (showing the $\langle 1\bar{1}00 \rangle$ component) superimposed. (c) GSFE of prismatic $\langle a \rangle$ slip calculated using DFT and various interatomic potentials [127], along with the atomistic mechanism for prismatic slip via a double cross-slip process of stable basal dislocations under a resolved shear stress on the orthogonal prismatic plane, obtained from NEB simulations with the MLIP_NNP potential [51]. (d) MD simulations on surface nucleation of pyramidal II $\langle c+a \rangle$ dislocations in a Mg single crystal under c-axis compression [128]. (e) Out-of-plane $\langle c+a \rangle$ slip mechanisms, including pyramidal-to-basal transitions and pyramidal cross-slip [22]. (f) Peierls stresses of various Mg solid-solution alloys predicted using the Peierls–Nabarro model parameterized by DFT results [129], with the black line indicating the reference value for pure Mg. Reprinted with permission from publishing houses.

Dan and Trinkle [133] performed first-principles calculations of core energies for isolated basal and prismatic screw dislocations in Mg using the energy density method. This approach enabled accurate evaluation of dislocation energetics, overcoming limitations of classical approaches.

In addition to DFT-based investigations, MD simulations have been widely employed to explore basal and prismatic dislocation dynamics in Mg. Uranagase and Matsumoto [134] applied MD simulations using the EAM_Mendelev potential [45] to evaluate the activation free energy of basal and prismatic dislocation loop nucleation in Mg. By constructing collective variables for the nucleation process, they revealed a linear relationship between enthalpic and entropic contributions, highlighting the temperature-dependent differences between basal and prismatic slip mechanisms. Itakura et al. [135] conducted an atomistic study using DFT and MD to investigate the cross-slip process of a screw $\langle a \rangle$ dislocation from the basal to prismatic plane in Mg. They computed the Peierls energy landscape and applied a line tension model to estimate the activation enthalpy, showing good agreement with experimental values. Their MD simulations with the EAM_Mendelev potential further revealed a temperature dependence of cross-slip behavior, characterized by jerky motion at low temperatures and smoother glide at elevated temperatures.

It has been noted that many classical semi-empirical interatomic potentials artificially predict a local energy minimum along the GSFE line for prismatic $\langle a \rangle$ slip [57]. This results in the erroneous stabilization of screw dislocations on the prismatic plane. In contrast, MLIPs trained on DFT data eliminate this artifact and correctly predict that prismatic $\langle a \rangle$ screw dislocations are unstable, while edge dislocations remain stable, as shown in Fig. 5(c) [51]. Stricker and Curtin [127] used a DFT-trained MLIP_NNP [51] to investigate prismatic slip in Mg, particularly focusing on $\langle a \rangle$ dislocations. They showed that prismatic slip occurs via a double-cross-slip mechanism involving basal dislocations, where the stress-dependent energy barrier was calculated using NEB, see Fig. 5(c). Building on this work, Liu et al. [136] investigated a low-temperature instability in prismatic slip using the MLIP_NNP potential. They found that the simulations reproduce experimental athermal flow behavior and identified a critical stress beyond which prismatic glide dominates over basal-prismatic double-cross-slip. More recently, Liu and Curtin [137] proposed a new mechanism for thermally activated prismatic slip based on kink nucleation at screw-to-non-screw transitions in dislocation loops using MD with the validated MLIP_NNP, reproducing experimentally observed activation barriers and dislocation velocities.

4.2. Pyramidal $\langle c+a \rangle$ dislocations

Pyramidal slip systems are essential for enabling plastic deformation along the c-axis, a prerequisite for ductility in Mg. These systems involve dislocations with Burgers vectors of $\langle c+a \rangle$ gliding on pyramidal first-order (pyramidal I) and second-order (pyramidal II) planes. Li and Ma [138] conducted MD simulations using the EAM_Liu potential to investigate pyramidal I slip in Mg. They discovered an unconventional slip mechanism involving two partial dislocations with mixed $\langle c \rangle$ and $\langle a \rangle$ components that glide independently to form a stacking fault. Nogaret et al. [139] conducted atomistic simulations to study edge and screw $\langle c+a \rangle$ dislocations in Mg using EAM_Liu and EAM_Mendelev potentials, revealing temperature-dependent transitions in dislocation core

structures and a significant decrease in CRSS at room temperature, facilitating dislocation glide.

As with prismatic slip, semi-empirical EAM potentials often introduce artifacts in predicting pyramidal dislocation behavior, particularly in dissociation and gliding mechanisms [57]. Ghazisaeidi et al. [140] studied the core structures of $\langle c+a\rangle$ edge and screw dislocations in Mg using DFT, revealing that both dislocations dissociate into two $\frac{1}{2}\langle c+a\rangle$ partials on pyramidal II planes. They assessed the performance of MEAM_Kim, EAM_Liu, and EAM_Mendelev potentials with their DFT results, showing MEAM_Kim closely reproduced the DFT results. Srivastava et al. [141] employed atomistic simulations using MEAM_Wu and MEAM_Kim potentials to uncover the mechanisms controlling plasticity in Mg, focusing on pyramidal I and II $\langle c+a\rangle$ screw dislocations. They discovered a new glide mechanism involving atomic shuffling that leads to the formation of stable super-jogs, which exert a strong drag effect, explaining the experimentally observed work-hardening, low ductility, and anomalous thermal-hardening in Mg. Recently, Sun et al. [142] investigated the core structure of edge $\langle c+a\rangle$ dislocations on the pyramidal I plane in Mg under the combined compressive normal stress and shear using MD with the MEAM_Wu potential. They discovered a novel core reconstruction that significantly lowers the Peierls stress and enhances the mobility of $\langle c+a\rangle$ dislocations.

The relative importance of pyramidal I vs. II $\langle c+a\rangle$ dislocations in mediating c-axis deformation has been widely debated. Fan and El-Awady [143] conducted MD simulations using the MEAM_Kim potential to investigate the formation and slip characteristics of $\langle c+a\rangle$ dislocations, comparing pyramidal I and II planes. Their results suggest that pyramidal I dislocations play a predominant role in c-axis compression, challenging previous experimental interpretations that favored pyramidal II slip. Ding et al. [144] performed DFT calculations on the GSFE lines of pyramidal $\langle c+a\rangle$ slip and investigated their dissociation mechanisms. They found that $\langle c+a\rangle$ dislocations form more readily on the pyramidal I plane than on the pyramidal II plane in Mg. In contrast, Kumar et al. [145] combined high-resolution TEM, DFT, and atomistic simulations using the MEAM_Wu potential to investigate pyramidal $\langle c+a\rangle$ dislocations in Mg. They showed that pyramidal II dislocations can dissociate into two equal partials, which are glissile under stress, while pyramidal I dislocations of similar character become sessile. Their work confirmed the experimentally observed dislocation configurations and clarified the differences in their mobility. Similarly, Li et al. [146] utilized MD simulations using the MEAM_Wu potential to explore the tension-compression response of pyramidal $\langle c+a\rangle$ dislocations in Mg. They discovered that pyramidal I dislocations exhibit strong tension-compression asymmetry, originating from their asymmetric partials, which cause the core to contract under compression and expand under tension, a phenomenon not observed for symmetrical pyramidal II and basal dislocations. Nitol et al. [28] developed a machine learning MLIP_NNP for pure Mg to investigate $\langle c+a\rangle$ dislocation slip and found that pyramidal II slip is preferred over pyramidal I slip under stress.

Atomistic simulations have also been pivotal in interpreting in-situ mechanical testing results. Yu et al. [147] employed in-situ TEM tensile tests and MD simulations using the EAM_Liu potential on Mg single crystals and nanoparticles to reveal a pronounced nanoscale size effect on plastic anisotropy. When sample dimensions were reduced below 100 nm, the CRSS anisotropy between basal and non-basal slip systems diminished substantially, enabling concurrent activation of basal, prismatic, and pyramidal $\langle c+a\rangle$ slip. This transition led to homogeneous plastic flow with ultrahigh strength ($\sim$2 GPa) and enhanced ductility (up to $\sim$30% uniform elongation), attributed to increased dislocation interactions, cross-slip, and surface nucleation of non-basal dislocations, thereby overcoming the typical strength–ductility trade-off in Mg. Liu et al. [148] utilized in-situ TEM compression tests and atomistic simulations using the MEAM_Wu potential to investigate the compression of submicrometer-sized Mg pillars along the c-axis. They demonstrated that $\langle c+a\rangle$ dislocations can accommodate large plasticity by gliding on both pyramidal I and II planes, leading to the "smaller is stronger and more ductile" phenomenon in Mg. Recently, Jeong et al. [128] combined in-situ TEM compression tests of c-axis oriented Mg nanopillars with atomistic simulations using the optimized MEAM_Wu potential [149] to study non-basal plasticity mechanisms at large strains, see Fig. 5(d). They found that initially active glissile pyramidal II $\langle c+a\rangle$ dislocations become impeded through interactions that form sessile basal stacking faults, leading to stress accumulation, dislocation avalanches, and eventual deformation twinning.

4.3. Out-of-plane $\langle c+a\rangle$ slip

While pyramidal $\langle c+a\rangle$ slip is critical for activating plasticity along the c-axis in Mg, it is not always confined to a single crystallographic plane. Out-of-plane mechanisms, such as transitions between pyramidal and basal planes and cross-slip between different pyramidal planes, are increasingly recognized as key factors governing dislocation mobility, work hardening, and overall ductility in Mg and other HCP metals. Understanding these processes at the atomic scale is essential for interpreting experimental observations and developing strategies to improve mechanical performance.

The stability of $\langle c+a\rangle$ dislocations in Mg has been examined using MD simulations, as illustrated in Fig. 5(e). Wu and Curtin [150,151] performed long-time MD simulations with the MEAM_Wu potential and revealed that $\langle c+a\rangle$ dislocations in Mg can transform into basal-dissociated sessile configurations. They proposed that this intrinsic transformation explains the work hardening and low ductility of Mg, suggesting that suppressing the pyramidal-to-basal transition could be a promising approach to enhance ductility. Later, Wu, Yin, and Curtin [152] combined anisotropic elasticity theory with DFT-calculated SFEs to analyze the energetics of dislocation transformations in six HCP metals. They found that climb dissociation of $\langle c+a\rangle$ dislocations to the basal

plane is energetically favorable across all cases, indicating a common mechanism that may limit ductility in HCP systems. Yang et al. [153] further examined the dissociation behavior of edge and screw $\langle c+a\rangle$ dislocations on pyramidal I and II planes in Mg using the MEAM_Wu potential. Their simulations showed that proper energy minimization before relaxation at finite temperatures is essential to retain in-plane dissociation; otherwise, high local stress concentrations can drive the dislocations to dissociate onto the basal plane. Nitol et al. [28] performed MD simulations using their MLIP_NNP to investigate $\langle c+a\rangle$ dislocation slip in Mg, showing that basal-dissociated $\langle c+a\rangle$ dislocation cores are mobile, challenging previous assumptions about their sessility. More recently, Matsumoto et al. [154] performed MD simulations using the optimized MEAM_Wu potential [149] to examine the migration behavior of basal-dissociated pyramidal II edge $\langle c+a\rangle$ dislocations in Mg. They found these dislocations, previously thought to be sessile, could migrate via a mechanism involving periodic Shockley partial exchange, highlighting unexpected mobility even at low temperatures.

The cross-slip mechanisms of $\langle c+a\rangle$ dislocations in Mg have been investigated using atomistic simulations, see Fig. 5(e). Tang and El-Awady [155] performed large-scale MD simulations using EAM potentials to study $\langle c+a\rangle$ dislocation-mediated plasticity in Mg single crystals under c-axis loading. They found that $\langle c+a\rangle$ dislocations nucleate on pyramidal I planes, mediated by atomic shuffling, and subsequently transition to slip on pyramidal II planes via cross-slip of screw segments or cooperative slip of edge segments. Wu and Curtin [156] examined $\langle c+a\rangle$ dislocation cross-slip in Mg using the MEAM_Wu potential based on NEB calculations. They discovered a unique cross-slip mechanism controlled by partial dislocation behavior and close core energy differences, rationalizing tension-compression asymmetry in Mg and similar HCP metals. Buey and Ghazisaeidi [157] employed MD simulations using the MEAM_Wu potential to explore the cross-slip behavior of $\langle c+a\rangle$ screw dislocations in Mg across pyramidal I and II planes at various temperatures. They identified a metastable compact core that enables cross-slip between the two pyramidal planes and found that pyramidal II slip is preferred at room temperature, suggesting temperature-dependent cross-slip behavior. Itakura et al. [158] conducted ab-initio calculations to investigate the cross-slip mechanism of pyramidal $\langle c+a\rangle$ screw dislocations in Mg. They discovered a novel non-planar stacking fault migration mechanism allowing dislocation motion between planes without classical cross-slip, reconciling experimental observations of slip traces with computational predictions. Zhang et al. [159] performed atomistic simulations using the MEAM_Wu potential to systematically examine the slip and cross-slip behavior of $\langle c+a\rangle$ screw dislocations on various planes in Mg. A key finding was the identification of a plausible new slip system on $\{\bar{1}2\bar{1}1\}$ planes, which has a low Peierls stress, in addition to observing frequent cross-slip among pyramidal I and II planes. Recently, Liu and Yin [160] proposed a force-correction method to eliminate the surface effects, thus enhancing the accuracy of DFT calculations of screw dislocations in Mg. They revealed that multiple metastable $\langle c+a\rangle$ core configurations exist on pyramidal planes, suggesting low energy barriers for cross-slip.

4.4. Solute effects on dislocation motion

The influence of solutes on dislocation-mediated plasticity in Mg has been extensively investigated using DFT, which offers the accuracy needed to resolve atomistic interactions. In particular, solid-solution alloying can either promote non-basal plasticity or suppress basal slip, thereby tailoring strength, ductility, and anisotropy. Datta et al. [161] used DFT calculations to analyze the stability of different stacking sequences in Mg–Zn–Y alloys. They found that Y stabilizes long-period stacking structures, while Zn reduces the basal SFE, leading to improvements in the mechanical properties of the alloys. Yasi et al. [162] performed DFT calculations and developed a predictive mesoscale model for solid-solution strengthening on the basal plane in Mg, replacing classical elasticity theory. They proposed a "strengthening design map" that includes 29 different solutes, which was validated with experimental data for common solutes such as Al and Zn. Pei et al. [129] utilized DFT-calculated GSFE to develop a computationally efficient method to predict basal dislocation properties in Mg alloys. They classified solutes into strengthening or softening categories based on their impact on Peierls stress, enabling high-throughput screening for alloy design as shown in Fig. 5(f). Yin et al. [163] used DFT to compute SFEs in Mg–Y, Mg–Al, and Mg–Zn alloys with different solute concentrations. They found that reductions in SFE do not directly correlate with enhanced $\langle c+a\rangle$ activity, challenging the prevailing assumption that the basal I1 stacking fault correlates with ductility and highlighting the need for more nuanced mechanistic models for ductility enhancement. Tehranchi et al. [164] applied a parameter-free model that incorporated a misfit strain contribution and a stacking fault interaction term into the Peierls–Nabarro framework to predict solute strengthening of basal slip in Mg alloys. Their model, validated by DFT and experiments, enables rapid estimates of strengthening effects for various solutes. Buey et al. [165] used DFT to investigate solute strengthening in Mg–Y alloys by computing interaction energies between solutes and $\langle c+a\rangle$ edge dislocations. They modified the solute–dislocation interaction model to account for core structural changes and demonstrated that Y reduces the CRSS ratio between pyramidal and basal slip, thereby enhancing plastic isotropy and ductility. Fang et al. [166] employed first-principles calculations to study interactions between various solutes and basal screw dislocation cores in Mg alloys. They found RE and Ca solutes can hinder dislocation dissociation, alter stacking fault widths, and induce non-planar dislocation cores, contributing to improved alloy strength and ductility. Fellinger et al. [167] used solid-solution strengthening models parameterized with DFT-computed solute–dislocation interaction energies to identify solutes that reduce yield strength anisotropies in Mg. They identified several RE and non-RE solutes, including Gd and Y, that could potentially improve ductility by lowering the ratio of non-basal to basal CRSS. More recently, Niazi and Curtin [168] explored the strengthening of pris-

matic edge dislocations in Mg–Zn alloys through cross-core solute diffusion. Using first-principles calculations and solute-strengthening theory, they found that while cross-core diffusion contributes significantly to strengthening, it accounts for only about 30% of the experimentally observed strength increase at high temperatures.

In addition to DFT-based studies, atomistic simulations have also been employed to directly evaluate solute effects on dislocation mobility using MD and MS approaches. Kim et al. [169] performed MD simulations to demonstrate that Y addition increases the CRSS of basal slip more than non-basal slip, thereby reducing the anisotropy and activating $\langle c+a \rangle$ slip in Mg-Y alloys. Later, Kim et al. [170] proposed that the underlying mechanism for the reduction of CRSS anisotropy is the stronger solute-dislocation binding tendency of solute atoms on basal slip planes compared to non-basal planes, which they verified with atomistic simulations and experiments. Similar studies have been conducted by the same research group [171–173], in which various binary and ternary Mg-based MEAM potentials were developed and applied to study solute effects. These works consistently demonstrated that carefully selected solute additions can reduce overall CRSS anisotropy and thus facilitate the activation of non-basal slip systems.

Solutes can also promote out-of-plane dislocation motion, particularly by facilitating cross-slip of $\langle c+a \rangle$ dislocations, which plays a critical role in enhancing ductility in Mg alloys. Yasi et al. [174] developed a first-principles statistical model to predict thermally activated cross-slip stresses, showing that alloys containing Sc, K, and Na could achieve lower forming temperatures than pure Mg. Following this, Yasi et al. [175] constructed a geometry-based model from first-principles data to predict thermal cross-slip stress, which successfully predicted that alloys with Ca, Y, and Zr could similarly reduce cross-slip stresses. Wu et al. [22] proposed a mechanistic theory, supported by DFT calculations and TEM observations, that enhanced ductility in Mg alloys stems from solute-accelerated $\langle c+a \rangle$ cross-slip and multiplication, which help prevent the buildup of immobile dislocation structures. Ahmad et al. [176] extended the solute-accelerated cross-slip theory by including multiple solutes and validating predictions with DFT and experimental data. They identified composition windows for ductile behavior and guided the design of RE-free high-ductility Mg alloys. Ding et al. [144] used DFT to investigate the origins of $\langle c+a \rangle$ dislocations and their dissociation mechanisms, finding that Y additions promote dissociation on pyramidal II planes, thereby facilitating their activation over pyramidal I in Mg–Y alloys. More recently, Brodie and Ghazisaeidi [177] employed DFT combined with the quasi-harmonic approximation to calculate the temperature-dependent Gibbs Free Energy of stacking faults in pure Mg and Mg-Al and Mg-Ca alloys. Their findings reveal that while pyramidal II SFE is lower than pyramidal I in pure Mg over a wide temperature range, the addition of Al or Ca solutes significantly reduces the pyramidal I SFE, making it more stable at all temperatures and lowering the cross-slip energy barrier.

MD simulations have also been widely employed to investigate how solutes influence the motion and transformation of $\langle c+a \rangle$ dislocations in Mg alloys. Ahmad et al. [178] performed MD simulations using their MEAM potential [179] to investigate $\langle c+a \rangle$ dislocation transitions in Mg-Y alloys. They found that while Y lowers the overall dislocation energy, it does not affect the transition mechanism or barrier, suggesting that enhanced ductility is not due to stabilization of pyramidal $\langle c+a \rangle$ dislocations. In a subsequent study, Ahmad et al. [149] analyzed the energetics of double-cross-slip of $\langle c+a \rangle$ screw dislocations on pyramidal I planes using NEB and MD simulations. They found that at higher solute concentrations, pyramidal I becomes energetically favorable, altering the dominant slip system and placing an upper limit on beneficial solute additions. Utt et al. [180] combined MC and MD simulations to explore solute segregation effects on dislocation behavior in Mg-Y alloys using the same MEAM potential. They reported that random solute distributions have little influence on the pyramidal-to-basal transition, whereas the formation of solute-rich clouds around dislocations effectively suppresses this transition, thereby stabilizing glissile motion and enhancing ductility. More recently, Shi et al. [181] integrated slip-trace analysis of a polycrystalline Mg–Zn alloy under tension with MD simulations using a MEAM potential [182]. They observed increased activation of pyramidal II $\langle c+a \rangle$ slip and secondary mechanisms such as twinning and cross-slip at higher strains, which they attributed to the multiple deformation pathways enabled by Zn additions.

5. Twinning

Twinning in Mg and its alloys has long been recognized as a key deformation mode accommodating strain along the *c*-axis of the HCP structure, complementing dislocation slip [185]. Upon activation during deformation, twinning induces pronounced texture evolution, substantial internal stress redistribution, and a marked increase in hardening rate that is not typically observed in the higher-symmetry cubic metals [15]. As a result, the mechanical behavior of Mg and other HCP crystals is considerably more complex than that of cubic metals, see the schematic of twinning in HCP crystals (Fig. 6(a)). Over the past two decades, extensive experimental and theoretical investigations have significantly advanced our understanding of twin nucleation, propagation, and interaction with defects, even in three dimensions [186,187]. In this section, we focus on twin nucleation and the central debate over twinning mechanisms, while twin thickening and the associated TB migration are discussed in Section 6 (6.1.3).

5.1. Twin nucleation

In hexagonal metals, twin nucleation cannot be explained by the conventional pole mechanism involving the glide of a single twinning dislocation, since an isolated twinning dislocation cannot exist within the HCP lattice. Moreover, homogeneous nucleation of twins within a grain is both energetically unfavorable and kinetically constrained, as it requires

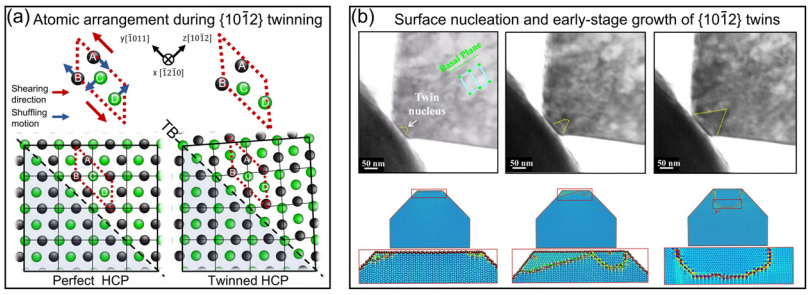

Fig. 6. Twinning mechanisms in Mg. (a) Atomic configurations and four-atom supercell shape of the perfect HCP lattice and the twinned HCP configuration during {10$\bar{1}$2} twinning shear deformation [183]. (b) Nucleation and early-stage growth of {10$\bar{1}$2} twins in Mg nanopillars [184]. Top: *In situ* compression tests parallel to the basal plane showing twinning events in a truncated wedge-shaped Mg pillar with a 100 nm top surface. Bottom: MD simulations illustrating twin nucleation at the top-surface corners, followed by propagation and growth. Reprinted with permission from publishing houses.

the activation of a zonal dislocation spanning multiple atomic layers. Wang et al. [188] investigated {10$\bar{1}$2} twin nucleation in Mg using DFT and a semi-empirical potential, revealing a glide–shuffle mechanism that involves both the glide of twin dislocations and atomic shuffling in the twinned layer. Subsequently, Wang et al. [189] reported an unconventional pure-shuffle mechanism for {10$\bar{1}$2} twin nucleation at GBs, attributed to high stress concentrations and pre-existing GB dislocations. Ishii et al. [183] employed DFT-NEB calculations and demonstrated that {10$\bar{1}$2} twin nucleation is likely governed by local atomic shuffling with a relatively small activation volume, making it highly sensitive to temperature and applied strain rate.

In situ microscopy and atomistic simulations have revealed that {10$\bar{1}$2} twin embryos form in regions of stress concentration through heterogeneous nucleation at GBs, prior twins or dislocation pile-ups, followed by rapid propagation mediated by disconnection motion along the TB [188,190–192]. Twin nucleation is believed to occur under applied stress through the transformation of GB defects into twinning partials, which subsequently coalesce to form a stable twin nucleus comprising multiple atomic layers [188]. The nucleation mechanism is influenced by both the atomic structure of the GB associated with its misorientation and the local stress state. Notably, low-angle boundaries have been shown by MD simulations and EBSD statistical analysis to exhibit a higher probability of twin nucleation [193]. Using a probabilistic model, Beyerlein and Tomé [193,194] demonstrated that twin nucleation and variant selection are primarily driven by local stresses at the GBs, whereas twin propagation is governed by the resolved shear stress within the grain interior. As a result, it was suggested that grain orientation has a greater impact on twin propagation than on nucleation itself. The rate of twin nucleation can be described as a stochastic process due to fluctuations in local stress at the boundaries, arising from randomly occurring dislocation pile-ups, as well as variations in threshold stresses for nucleation caused by different local dislocation configurations and GB characteristics [190]. The average density of nuclei per unit boundary area was reported to increase with rising local stress. Striking examples are the surface nucleation of {10$\bar{1}$2} twins in single crystalline Mg nanopillars, revealed by *in situ* TEM mechanical testing and supported by MD simulations [184,195]. Crystal geometry and the resulting local stress distributions strongly influence early-stage twin growth, which is closely tied to the instability of plastic flow, see Fig. 6(b). Additionally, twin nucleation proceeds via a pure-shuffle mechanism involving prismatic–basal transformations [184].

Apart from {10$\bar{1}$2} twin nucleation, other twinning modes in Mg have also been investigated using atomistic simulations in detail. Li et al. [196] studied the nucleation and growth of {10$\bar{1}$1} compression twins in Mg single crystals using MD simulations. They revealed that twin embryos can nucleate at free surfaces through the cross-slip of prismatic $\langle a \rangle$ dislocations onto pyramidal planes, facilitated by basal stacking faults that reduce the required atomic shuffling. Beyond compression twins, new mechanisms have been uncovered for less common twinning systems. Wang et al. [197] reported a previously unidentified mechanism for {11$\bar{2}$2} twinning, which emerges through the interaction of co-zone {11$\bar{2}$1} variants. Their atomistic simulations showed that the merging of two {11$\bar{2}$1} TBs produces a coherent {11$\bar{2}$2} TB, independent of classical twinning dislocations. Alloying effects can further diversify twin nucleation behavior. Xiao et al. [198] combined DFT calculations and atomistic simulations to reveal that Y solutes promote the activation of the {11$\bar{2}$1} twin in Mg, a mode rarely observed in pure Mg. By enhancing shuffle displacements along the $< 1\bar{1}00 >$ direction, Y atoms lower the energy barrier for multi-layer twin embryo formation, making this twin competitive with the {11$\bar{2}$2} extension twin.

5.2. Twinning mechanisms

A central debate in the literature concerns the atomic-scale mechanisms responsible for twin growth, particularly the role of atomic shuffling in the migration of TBs vs. the motion of twinning dislocations along the TB. Li and Ma [199] performed MD simulations using the EAM_Liu potential and proposed that coordinated atomic shuffles in the two {10$\bar{1}$2} layers of the parent lattice are responsible for the growth of {10$\bar{1}$2} twins without the need for dislocation processes on this twinning plane. This hypothesis sparked intense de-

bate [200,201] and underwent subsequent refinements through high-resolution TEM and atomic-scale modeling [184,202]. More recent studies have demonstrated the coexistence of shear-dominated disconnection motion with localized atomic shuffles. This suggests that both shear and shuffling contributions are necessary for TB migration, depending on local stress states and interface structure [183,187,203]. Advances in phase-field and crystal plasticity simulations have further elucidated the collective behavior of twins, including their interactions, growth anisotropy, and role in strain hardening [185,204,205]. Internal stresses and strains evolutions, and plasticity within twin and parent domains were reported in Mg alloys via double inclusion-based elasto-plastic self-consistent scheme [206,207]. Twin–GB interactions play a critical role in controlling twin propagation and transmission. Atomistic and phase-field studies have revealed the influence of structural facets, stress, and temperature on TB mobility [208,209]. At the polycrystalline scale, recent investigations showed how twin–GB interactions govern strain hardening and formability, while twin transmission propensity decreases with increasing grain misorientation [210,211].

The integration of atomic-scale insights with mesoscale models now provides a first glimpse of a coherent framework linking disconnection-mediated TB motion to macroscopic deformation, though open questions remain on the competition between multiple twin modes and the influence of alloying [197,198,212,213]. Overall, twinning in Mg exemplifies a multiscale deformation process, where atomic shuffling, interfacial disconnections, and long-range stress interactions are inseparably coupled.

6. Grain boundaries

GBs are 2D crystallographic defects that separate regions of differing lattice orientations and play a critical role in controlling the properties of Mg and its alloys, influencing phenomena such as recrystallization, grain growth, and plastic deformation [17,214]. Depending on their crystallographic character and atomic arrangement, GBs can be broadly categorized into special low-energy boundaries, such as TBs, and high-energy general boundaries. While TBs often form during plastic deformation via twinning, as introduced in Section 5, and exhibit highly ordered structures with relatively low interfacial energies, general GBs encompass a wide variety of symmetric and asymmetric tilt and/or twist boundaries with more disordered atomic configurations and higher energies.

Recent advances in high-resolution microscopy, first-principles calculations, and atomistic simulations have enabled atomic-scale characterization of GB structures, segregation behaviors, and migration mechanisms in Mg and its alloys. These studies have revealed that both TBs and general GBs can undergo solute-induced structural transitions and exhibit distinct migration modes that critically influence macroscopic mechanical response.

6.1. Twin boundaries

6.1.1. Structures and energies

The structures and energies of TBs in Mg, particularly the common $\{10\bar{1}2\}$ extension TB and the $\{10\bar{1}1\}$ contraction TB, have been extensively investigated using atomic-scale modeling. Wang et al. [43] performed first-principles calculations to determine the interfacial energies of four types of TBs in Mg, including $\{10\bar{1}1\}$ reflection TB, $\{10\bar{1}1\}$ glide TB, $\{10\bar{1}2\}$ reflection TB, and $\{10\bar{1}2\}$ glide TB. TB energies yield values of 85.5 mJ/m^2 for the $\{10\bar{1}1\}$ reflection TB, 81.0 mJ/m^2 for the $\{10\bar{1}1\}$ glide TB, 118.1 mJ/m^2 for the $\{10\bar{1}2\}$ reflection TB, and 120.0 mJ/m^2 for the $\{10\bar{1}2\}$ glide TB. Kumar et al. [219] used DFT to study the structures and energies of $\{10\bar{1}1\}$, $\{10\bar{1}2\}$, and $\{10\bar{1}3\}$ TBs in six HCP metals, including Mg. They found that TB formation is generally associated with the creation of excess volume. For HCP metals with $c/a < \sqrt{8/3}$, the $\{10\bar{1}2\}$ TB exhibits higher formation energy than $\{10\bar{1}1\}$ and $\{10\bar{1}3\}$ TBs, whereas the opposite trend occurs in metals with $c/a > \sqrt{8/3}$. Pei et al. [38] combined DFT with atomistic simulations to systematically explore possible intrinsic $\{10\bar{1}1\}$ and $\{10\bar{1}2\}$ TB structures in Mg, see Fig. 7(a). By mapping energetics as a function of shear and shuffle parameters, they assessed mechanical stability against small distortions, resolving long-standing discrepancies between theory and experiment regarding glide versus reflection TB configurations. They found that the absence of glide TBs in experiments was a consequence of their mechanical instability, specifically the lack of any metastable configuration, rather than limitations in nucleation or growth mechanisms. Zhu et al. [220] employed DFT to define a strain-dependent energy for the $\{10\bar{1}2\}$ TB, quantifying the effects of external stress and solute segregation on TB stability under different strain paths. They demonstrated that solute selection based on electron work function can be used to deliberately stabilize or destabilize twins, consistent with qualitative experimental observations. Beyond the commonly reported tensile and compressive TBs, Lane et al. [221] used first-principles calculations to determine the energy and structure of a $\{11\bar{2}1\}$ TB in Mg. They demonstrated that this type of TB can form via basal dislocation glide without atomic shuffle and linked its boundary energy to the elastic constant C_{44}, as well as to the low CRSS of basal dislocations that comprise the twin. More recently, Zeng et al. [222] performed atomistic simulations using the EAM_Liu potential to characterize twin facets associated with 3D $\{10\bar{1}1\}$ twins in Mg. They identified coherent facets bounding non-equilibrium twins and semi-coherent facets formed after misfit dislocation rearrangement in equilibrium twins. They quantified facet stability and revealed how twinning dislocation line sense and arrangement control facet orientation, coherency, and mobility.

6.1.2. Solute segregation

Solute segregation at TBs in Mg alloys has been extensively investigated using a combination of atomic-scale microscopy and modeling, revealing that segregation patterns strongly influence TB structure, stability, and mobil-

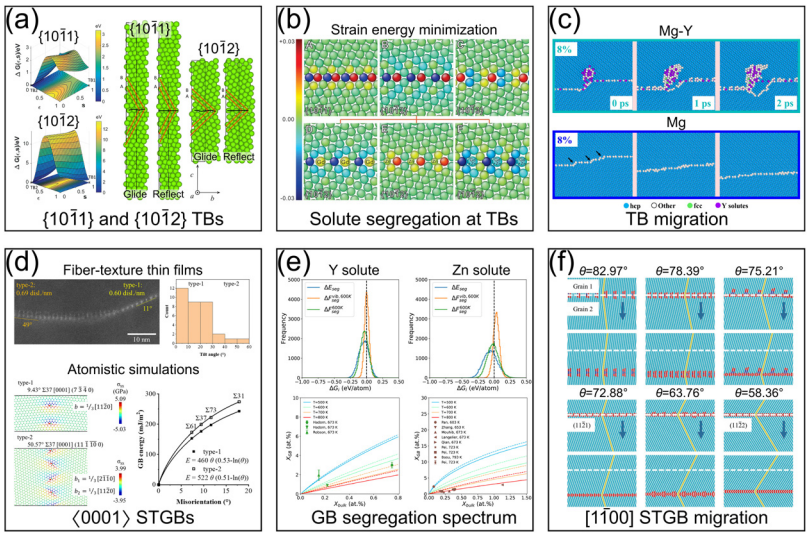

Fig. 7. Atomic-scale investigations of GBs in Mg and its alloys. (a) Structures and energies of the {10$\bar{1}$1} contraction TB and {10$\bar{1}$2} extension TB modeled using DFT and classical atomistic simulations [38]. (b) Periodic solute segregation at TBs driven by strain energy minimization, calculated with DFT [215]. (c) Migration of faceted {10$\bar{1}$2} TBs in Mg–Y alloys and pure Mg using MD simulations [216]. (d) Structures and energies of ⟨0001⟩ STGBs in sputter-deposited Mg thin films, modeled with the EAM_Liu potential [69]. (e) Segregation spectrum of Y and Zn solutes at GBs in polycrystalline Mg predicted using MEAM_Kim potentials, with comparison to Langmuir–McLean concentrations and experimental data [217]. (f) Migration of high-angle [1$\bar{1}$00] STGBs modeled with MD simulations using the EAM_Liu potential [218]. Reprinted with permission from publishing houses.

ity, thereby shaping twinning behavior and mechanical properties. Nie et al. [215] combined atomic-resolution STEM with DFT modeling to reveal periodic, ordered segregation of solutes such as Gd and Zn at {10$\bar{1}$1}, {10$\bar{1}$2}, and {10$\bar{1}$3} TBs, as shown in Fig. 7(b). The segregated solutes formed nanoscale structural units, referred to as "complexions" or "defect phases", that are thermodynamically stable only at TBs. These ordered arrangements effectively pinned TBs and reduced their mobility, leading to annealing-induced strengthening. Subsequent studies demonstrated similar stabilization mechanisms. Zhao et al. [223] investigated the energetics of alternating Nd/Ag columns at TBs in Mg, computing relative energies for filling compression/extension columns in {10$\bar{1}$2} and {10$\bar{1}$1} TBs. They showed that the experimentally observed co-segregation patterns lower TB energy and impose kinetic drag, thereby reducing TB mobility. Chen et al. [224] used DFT to evaluate Ag segregation at {10$\bar{1}$1}, {10$\bar{1}$2} and {10$\bar{1}$3} TBs, identifying site-specific motifs: substitutional occupation at compression sites for {10$\bar{1}$1}/{10$\bar{1}$2} TBs and a hybrid substitutional–interstitial arrangement at {10$\bar{1}$3} TBs. Their findings rationalized high-angle annular dark-field (HAADF) intensity variations and zig-zag periodic segregation patterns. Xie et al. [225] combined HAADF-STEM with DFT to reveal periodic superstructures formed by solute segregation at {10$\bar{1}$2} TBs in Mg alloys, characterized by alternating solute-enriched and solute-depleted columns. Their DFT calculations reproduced the observed periodicities and confirmed that energetically preferred solute occupations drive the self-assembly of ordered TB defect phases. He et al. [226] combined DFT with a quasi-random structure approach to examine solute concentration effects on TB energy, showing that larger RE solutes such as Gd, Er, Y, and Nd significantly reduce {11$\bar{2}$1} TB energy by relaxing local strains, thereby promoting {11$\bar{2}$1} twinning observed in Gd-rich alloys, which explains the experimentally observed profuse {11$\bar{2}$1} twinning in Gd-rich alloys. In a follow-up study, He et al. [227] provided further insight into segregation mechanisms. By analyzing differential electron charge density and Bader analysis, they showed that large *p*-block solutes (e.g., Bi, Pb) preferentially segregate to compression sites in {10$\bar{1}$1} TBs but avoid {10$\bar{1}$2} TBs, contradicting simple size-misfit rules but correlating well with the experimentally measured HAADF intensities. They attributed this behavior to chemical bonding and electronic configuration effects rather than elastic-strain minimization. More recently, Yang et al. [228] studied a 61°/25° asymmetric tilt boundary on {10$\bar{1}$2} TBs in Mg–Gd–Zn alloys. Combining HAADF-STEM with atomistic simulations (MEAM_Wu potential), they showed that the interactions between ⟨*a*⟩ dislocations and TB can generate this unusual morphology. DFT demonstrated that Gd and Zn preferentially segregate to the cores of aggregated dislocations and interfacial interstices, respectively, stabilizing the structure.

A broader body of DFT studies has systematically explored segregation across various solute elements at TBs in Mg. Shi et al. [229] computed segregation energies of Al, Zn, Ca, Sn, Y, Gd, and Nd solutes at {10$\bar{1}$2} TBs using DFT, finding that RE elements and Ca exhibit much stronger segregation tendencies than other elements. Zhang et al. [230] calculated segregation energies and solute-diffusion activation enthalpies at {10$\bar{1}$2} TBs in 21 Mg binary systems, evaluating both thermodynamic segregation driving forces and kinetic accessibility, and constructing a "design map" to guide solute selection for controlling twin density and mobility. Pei et al. [37] calculated segregation energies for 23 solutes at {10$\bar{1}$2} and {10$\bar{1}$1} TBs.

Using Voronoi analysis to separate volumetric contributions, and applying the Langmuir–McLean isotherm, they translated energies into solute coverages and proposed coverage-based descriptors for TB strengthening. Chen and Song [231] developed a computational two-factor model to assess solute segregation at $\{10\bar{1}2\}$ TBs by combining first-principles segregation energy calculations with statistical analysis. They computed segregation energies for 20 alloying elements and correlated them to two key factors: atomic size misfit and electronegativity difference relative to Mg.

Other DFT works expanded segregation studies into related property domains, such as corrosion and hydrogen embrittlement. Ma et al. [232] developed a first-principles-based anodic dissolution model to isolate how $\{10\bar{1}1\}$, $\{10\bar{1}2\}$, and $\{10\bar{1}3\}$ TBs affect Mg corrosion, showing TBs raise surface energy density and accelerate dissolution in proportion to interfacial length per area. They computed that certain alloying additions (As, Cd, Hg, Zn, Sn) at TB-containing surfaces can lower current density and mitigate the rate. Huang and Nie [233] studied solute–hydrogen co-segregation at $\{10\bar{1}2\}$ TBs and evaluated the effect on interfacial cohesion. They found H bonds strongly with Li/Ca/Mn/Zr/REs, forming solute-H clusters attracted to TBs that reduce cohesion via electron transfer, while Al/Sn/Bi/Zn/Ag show weak H bonding and can discourage H segregation. They connected $d-p$ electronic interactions to TB strengthening in H-free cases and quantified embrittlement trends when H is present.

6.1.3. Mechanical responses

The migration of TBs in Mg has been widely studied using atomistic simulations with semi-empirical potentials to uncover the mechanisms governing their motion. Wang et al. [192] performed MD simulations with the EAM_Liu potential on serrated $\{10\bar{1}2\}$ TBs, comprising alternating coherent TB segments and basal–prismatic plane serrations, migrate via the combined glide and climb of twinning dislocations plus atomic shuffling. The geometry and density of serrations were found to control twinning/detwinning kinetics and hardening behavior. Spearot et al. [234] used MD (MEAM_Wu potential) to study $\{10\bar{1}2\}$ TB migration in both 2D and 3D models. They demonstrated that nucleation, lateral growth, and coalescence of disconnection terraces govern shear-driven TB motion, where a velocity law was established as a function of temperature and shear stress. They found that 2D models do not capture activation events, emphasizing the necessity of fully 3D simulations. Chen et al. [235] reported a reversible local HCP-to-FCC transformation during $\{10\bar{1}2\}$ TB migration, driven by misfit strain, using MD simulations (EAM_Liu potential). They computed transformation barriers and showed transient FCC layers temporarily hinder TB migration via shear-and-shuffle pathways, supporting a shuffling-dominated twinning mechanism rather than classical zonal dislocation models. Recently, Yu et al. [236] applied the NEB method using the MEAM_Wu potential to quantify the migration energy barrier of $\{10\bar{1}2\}$ TBs in Mg under varying non-glide stress conditions. They discovered that compressive normal stresses reduce the migration barrier by modifying the most favorable twinning disconnection configuration, whereas other non-glide stresses can increase or decrease the barrier depending on their effect on atomic shuffling. In addition to empirical models, Li et al. [237] applied DFT to map the migration energy landscape of $\{10\bar{1}1\}$ and $\{10\bar{1}3\}$ TBs in Mg. They modeled migration as the nucleation and glide of 2-layer-height twinning disconnections by simulating rigid-body shifts of TB planes to determine energy barriers under various shear strain orientations. They found that nucleation requires shear components along both the twinning and the normal directions. Since glide barriers were lower than nucleation barriers, twinning disconnection nucleation was identified as the rate-limiting step for these TB migration modes.

Several studies have demonstrated that solute segregation exerts a strong pinning effect on TBs. Ge et al. [238] used DFT to show that Li preferentially occupies interface vacancies and forms coherent Li clusters along $\{10\bar{1}2\}$ TBs in Mg. Complementary MD simulations with the MEAM_Kim potential revealed that these clusters pin dislocations and increase the critical shear strain for TB migration, in agreement with their TEM observations. Tang et al. [239] performed MD simulations using the EAM_Liu potential to study the interaction of $\{10\bar{1}2\}$ TBs with point defects in Mg, finding that vacancies tend to reduce TB migration resistance (softening effect), whereas interstitials increase it (hardening effect) by being absorbed into the TB and forming clusters. Using the NEB method, they found that interstitials have lower migration barriers and therefore higher mobility along TBs compared to vacancies. Wang et al. [216] observed Y segregation at $\{10\bar{1}2\}$ TBs and basal–prismatic facets in Mg–Y alloys during room-temperature deformation via HAADF-STEM. MD simulations using an EAM potential demonstrated that such segregation configurations minimize local strain energy and create pinning points along the TB, thereby reducing its mobility under applied stress as illustrated in Fig. 7(c). Su et al. [240] combined atomic-resolution HAADF-STEM with MD simulations to study the dislocation-assisted evolution of $\{10\bar{1}3\}$ TBs in Mg. Experiments revealed that TB migration is often accompanied by the nucleation and glide of partial dislocations at the interface. MD simulations, based on the EAM_Liu potential, reproduced this process and showed that solute segregation to dislocation cores lowers the system's total energy and can either promote or inhibit TB migration depending on the segregation site. Somekawa et al. [241] used DFT to calculate segregation energies of Al, Zn, Ca, and Y at $\{10\bar{1}2\}$ TBs. They linked these values to migration barriers obtained from NEB calculations, showing that solutes strongly bound to compression sites (e.g., Ca, Y) significantly raise migration barriers, while weakly binding solutes such as Al have minimal influence.

Beyond mobility, solutes also affect TB cohesion and fracture resistance. Xi et al. [242] investigated the effect of 21 alloying elements on the cohesion of the $\{10\bar{1}1\}$ TBs, comparing segregation energies at TBs and free surfaces to identify solutes that strengthen or embrittle boundaries and proposing a design framework for crack suppression. Tsuru et al. [243] integrated DFT with interfacial fracture mechanics and

experimental fracture toughness measurements in Mg binary alloys, showing that Zr enhances TB cohesion through strong $p-d$ hybridization with Mg, consistent with improved fracture toughness. Li and Chen [244] systematically assessed how segregation of 16 solute elements affects the toughness and strength of $\{10\bar{1}2\}$ TBs in Mg using DFT, finding that elements like Ba and Li embrittle and weaken the TB, while Ca, rare earths, Zn, Al, and Ag toughen and strengthen it. The pinning effect was strongly site-dependent, with segregation at compression sites yielding greater strengthening than at extension sites.

6.2. Other grain boundaries

6.2.1. Structures and energies

Atomistic simulations enable the investigation of GB systems containing far more atoms than conventional DFT calculations, which are typically restricted to a few TBs and selected CSL GBs. Wang and Beyerlein [245] employed atomistic simulations with the EAM_Liu potential to determine the relaxed atomic structures of $[0\bar{1}10]$ STGBs in Mg over the full range of misorientation angles. They found that all boundaries exhibit ordered structures that can be grouped into six structural sets, each defined by a base boundary plane and an array of discrete intrinsic GB dislocations with a specific Burgers vector. The classification was shown to be robust across different c/a ratios and interatomic potentials, providing a crystallography-based predictive framework for GB structures. In a follow-up study, Wang and Beyerlein [246] analyzed $[1\bar{2}10]$ STGBs in Mg, identifying four low-energy coherent GBs, including basal and prismatic boundaries. Deviations from these orientations introduced ordered arrays of edge-type dislocations, with abrupt structural transitions occurring as misorientation switched between different base structures. Subsequent work expanded these structural maps to additional GB orientations, Liu and Wang [247] applied atomistic simulations to characterize both $\langle 0001\rangle$ tilt and (0001) twist GBs in Mg across rotation angles from 0° to 60°, mapping energy landscapes and identifying structural units. Both boundary types were described by ordered dislocation models, with a pronounced energy minimum at 30°. At this orientation, the tilt GB consists of arrays of Shockley partials on every basal plane, while the twist GB exhibits a stacking-faulted structure. Both were found to be highly mobile through collective partial glide, suggesting their role in promoting strong basal textures during grain growth. Ni et al. [248] further studied $[0\bar{1}10]$ STGBs in Mg using EAM_Liu and EAM_Mendelev potentials. They reported similar trends in GB energy versus misorientation, with cusps corresponding to specific TBs such as $\{11\bar{2}3\}$, and identified a unique crystallographic reorientation for the $\{11\bar{2}6\}$ TB. Experimental validation of these atomistic predictions was provided by Zhang et al. [69], who combined TEM observations of $\langle 0001\rangle$ tilt GBs in sputter-deposited Mg thin films with atomistic simulations using the EAM_Liu potential (Fig. 7(c)). They classified boundaries into type-1 and type-2, based on orientation relative to low-index planes. Type-2 GBs exhibited denser dislocation arrays and higher energies. Additionally, Ga from focused ion beam milling was found to segregate preferentially to dislocation cores, and simulations confirmed the energetic favorability of such segregation. While atomistic simulations reveal structural units and energetics across a wide misorientation range, DFT provides complementary insights into electronic structure and local stability. Xu et al. [249] investigated atomic configurations and energies of $[1\bar{1}00]$ and $[1\bar{2}10]$ STGBs in Mg using CSL models across the full misorientation range. They identified special boundaries corresponding to energy cusps and analyzed Bader charges, local energies, and stresses. Their results linked GB stability to modest charge and stress variations and revealed that, unlike covalently bonded materials, Mg GB energetics are governed more by geometric and dislocation arrangements than by strong electronic heterogeneity.

6.2.2. Solute segregation

Solute segregation in Mg alloys has been investigated across a wide spectrum of GBs, ranging from high-symmetry CSL boundaries to general GBs. Huber et al. [35] calculated segregation energies of solutes (Ag, Zn, Ti, Al, Cd, Zr, Y, Ca, Nd, Ce, La) to a $\Sigma 7$ $(12\bar{3}0)[0001]$ 21.8° GB in Mg via DFT. They found that segregation energies scale primarily with solute size and local GB site volume, allowing classification into "La-like" (large) and "Ag-like" (small) families. A pressure–volume–based model was proposed, later extended using MS with the EAM_Mendelev potential to predict segregation at general GBs beyond DFT reach. Huang et al. [250] applied atomistic simulations with the MEAM_Kim potential to basal–prismatic interfaces, finding that semi-coherent interfaces are more stable than coherent ones, with segregation energies strongly correlated to local hydrostatic tensile stress. Dislocation cores at semi-coherent interfaces acted as favorable trapping sites for Y. Several studies combined advanced characterization techniques with atomistic modeling to capture solute-induced GB transformations. Zhang et al. [251] combined HAADF-STEM imaging with DFT calculations to study a newly observed twin-like $\{33\bar{6}4\}$ tilt GBs in a Mg–Y alloy. They showed that this GB evolved from a $\{11\bar{2}1\}$ TB and stabilized via ordered Y segregation. Pei et al. [252] combined 3D APT with MS simulations using the MEAM_Kim potential to investigate solute segregation in Mg–Nd alloys, revealing pronounced inhomogeneity in Nd concentration not only between different GB orientations but also within the same GB plane. This work showed that these variations arise from local atomic rearrangements and site-specific excess free volumes, rather than solely from macroscopic GB character, highlighting the importance of atomic-level descriptors for predicting GB segregation in polycrystals. Yang et al. [253] combined atomic-resolution STEM and DFT calculations to reveal that segregation of RE solutes at partially coherent tilt GBs can trigger localized interfacial structural transformations into a Kagome lattice configuration, presumably a GB defect phase. DFT confirmed that solutes segregate preferentially to sites that minimize elastic strain energy, leading to an atomic shuffling process that converts embedded $\{10\bar{1}1\}$ triangular–quadrilateral motifs into topologically hexagonal–

triangular Kagome networks. Theoretical modeling further established the thermodynamic conditions for such transformations, highlighting solute-driven GB defect phase transitions as a pathway for interface property tuning. Zhou et al. [36] applied atomic-resolution STEM and DFT to construct GB defect phase diagrams in Mg–Ga alloys, showing that controlled Ga segregation can induce GB phase transformations that enhance cohesion. By triggering and tracking structural changes in individual GBs under different chemical conditions, they mapped stability regions for distinct GB defect phases and related them to improved tensile ductility in experiments. This approach demonstrates a thermodynamically grounded, defect-phase-diagram-based methodology for designing GB chemistry in Mg alloys. Xue et al. [254] combined experiments with DFT and MD simulations to reveal that site-specific Zn segregation at GBs in Mg–Al–Ca–Zn alloys modulates Al and Ca co-segregation, enhancing solute drag and activating non-basal $\langle c+a \rangle$ dislocations, which collectively hinder dynamic recrystallization and drive lamellar heterogeneous structure formation. Ganguly et al. [71] performed hybrid MD/Monte Carlo simulations with the EAM_Mendelev potential to study GB segregation in basal-textured Mg–Al polycrystals, calculating per-site segregation energy spectra and identifying unique bimodal distributions linked to special GB sites such as triple junctions and low-angle GBs. They further observed, at finite temperatures and high solute concentrations, segregation-induced GB structural transitions, including the formation of thermodynamically stable and metastable intermetallic phases. These atomistic insights into segregation spectra and defect phase formation extend understanding beyond dilute limits and have implications for tailoring GB chemistry and structure in Mg alloys.

Recent years have seen a rapid growth of machine learning methods to predict segregation energetics across diverse GBs. Wagih et al. [255] trained machine learning models on large-scale atomistic segregation datasets with local atomic environments of undecorated GB sites as descriptors to predict GB segregation energy spectra for polycrystals. They applied the models to over 250 binary alloys, including Mg alloys, creating a database that captures segregation anisotropy across GB character space. Messina et al. [256] performed atomistic simulations of Al segregation in 30 distinct $\langle 0001 \rangle$ STGBs, building a dataset to train machine learning models that could predict segregation tendencies directly from GB local atomic environments. Menon et al. [257] developed a multi-step framework for Y segregation at $[0\bar{1}10]$, $[1\bar{2}10]$, and [0001] STGBs. Using MS with the optimized MEAM_Wu potential [149] and verifying key sites with DFT, they generated per-site segregation spectra, incorporated entropic effects via MD-based thermodynamic integration, and trained a surrogate machine learning model. This approach reproduced experimental segregation trends at 500–800 K, demonstrating the role of entropy in GB segregation. Most recently, Xie et al. [217] integrated large-scale atomistic simulations using the optimized MEAM_Kim potentials with machine learning to predict segregation thermodynamics for multiple solutes (Nd, Ca, Y, Li, Al, Zn), commonly used in wrought Mg alloy sheets and extrusions, in polycrystalline Mg, see Fig. 7(e). By combining energetic (i.e., potential and vibrational free energies) and structural descriptors (i.e., atomic and flexibility volumes), their regression models captured skew-normal segregation energy and segregation free energy distributions. Comparing predicted Langmuir–McLean concentrations with experimental measurements, the study identified Nd as particularly prone to strong GB segregation, underscoring the combined value of physics-based descriptors and machine learning for GB engineering.

6.2.3. Mechanical responses

GB sliding and GB migration represent two distinct but often interconnected modes of boundary motion in Mg alloys. Sliding corresponds to tangential displacement of adjacent grains under shear and is strongly influenced by GB cohesion and solute segregation, while migration involves normal motion of the boundary driven by interfacial energy reduction and stored energy differences or shear coupling, governed by GB character and solute drag. Zhang [258] performed MD simulations with the EAM_Mendelev potential on $[10\bar{1}0]$ tilt GBs in Mg and found that shear deformation is dominated by coupled motion, namely tangential sliding accompanied by normal migration, mediated by GB twinning. The coupling coefficient matched theoretical predictions, though the detailed shear response varied with GB type, shear stress, and temperature. Somekawa and Tsuru [259] combined nanoindentation-based damping measurements with first-principles calculations to demonstrate that alloying elements tune GB cohesion: Li, with weak Mg bonding, promoted sliding, while RE elements suppressed it by stabilizing GB structures. Extending this idea, Somekawa et al. [260] used DFT to show that *p*-block elements such as Sn, Sb, and Bi lower GB energy and reduce GB cohesion and enhance sliding by weakening Mg–Mg bonds, whereas Al and Si strengthen cohesion and suppress sliding.

GB migration studies via atomic-scale modeling in Mg alloys emphasize the role of GB structure, disconnection mobility, and solute drag in texture evolution. Barrett et al. [261] combined EBSD with MD simulations (EAM_Liu potential) and showed that boundaries such as the newly observed $\{13\bar{4}0\}$ TB possess low energies and high mobilities, acting as preferential sites for subgrain rotation during dynamic recrystallization. MD simulations revealed highly mobile disconnections with wide cores, consistent with orientation selection observed experimentally. In a follow-up, Barrett et al. [262] studied how Y segregation affects GB energy and mobility during recrystallization in Mg using MD with the MEAM_Kim potential. They found that Y segregation reduces the energy differences between various $\langle a \rangle$ fiber GBs and thus the mobility anisotropy, preventing the rapid growth of specific orientations and weakening texture development. Nahhas and Groh [263] applied MS simulations with various semi-empirical potentials to model the mechanical response of a $\{10\bar{1}1\}$ STGB in pure Mg and Mg binary alloys, showing that in pure Mg, migration occurs via twinning dislocations, whereas in alloys, solute segregation pins GBs and sup-

presses migration. Mahjoub et al. [264] used DFT and NEB to quantify migration barriers and GB diffusion parameters for selected solutes, showing that strongly bound solutes reduce mobility while weakly bound ones have negligible effect, providing atomistic parameters for mesoscale models. Xing et al. [218] mapped transitions between sliding and migration in $[1\bar{1}00]$ STGBs using MD with the EAM_Liu potential. They showed that deformation mode depends on the lower of the two competing barriers: high-angle GBs favor migration (see Fig. 7(f)), low-angle ones favor sliding, and increasing temperature expands the sliding regime. The simulations clarified the atomic-scale disconnection modes involved and linked the invariant planes of migration to specific misorientation ranges, offering quantitative insight for controlling GB-mediated plasticity in fine-grained Mg.

The GB fracture behavior in Mg alloys has been reported using DFT and atomistic simulations. Mahjoub et al. [265] performed DFT calculations to investigate fracture behavior and cohesion in both a $\{10\bar{1}2\}$ TB and a non-symmetrical general GB in Mg, chosen to match experimentally observed fracture planes. This was the first DFT study of non-symmetrical GBs in Mg, requiring large supercells. They computed segregation energies for solutes of various sizes and assessed embrittlement potency, finding that smaller solutes tend to toughen GBs, while larger ones tend to embrittle. They showed that the general GB exhibited more complex cohesive behavior than the TB, emphasizing the need to model realistic, non-symmetrical interfaces. Xing et al. [266] performed MS simulations with an EAM potential to investigate crack–GB interactions in Mg, focusing on $[2\bar{1}\bar{1}0]$ asymmetric tilt, $(01\bar{1}0)$ twist, and $\langle 0001\rangle$ asymmetric tilt GBs. They varied misorientation and found that GB energy strongly influences whether the fracture is transgranular or intergranular, with low-energy GBs promoting crack penetration and high-energy GBs favoring crack deflection. The critical stress intensity factor for crack propagation was correlated with GB energy, and fracture mode transitions were linked to changes in local plasticity at the GB.

GBs often serve as heterogeneous nucleation sources of dislocations and twins in Mg. Uranagase and Matsumoto [267] performed MD simulations with the EAM_Mendelev potential of uniaxial tension and compression in Mg bicrystals containing $[1\bar{1}00]$ STGBs. Sixteen different misorientation angles were examined to correlate GB energy with mechanical response. They found that misorientation angle strongly influences the CRSS and the active deformation mode, with low-energy boundaries more prone to nucleating basal dislocations. The study also revealed clear tension–compression asymmetry in yield behavior, which was interpreted in terms of GB-mediated dislocation nucleation and changes in misorientation under elastic loading. Xu et al. [268] extended this to $[2\bar{1}\bar{1}0]$ STGBs, showing that GB misorientation governs whether deformation proceeds via twinning, basal slip, or mixed modes, again with tension–compression asymmetry linked to GB dislocations. Ma et al. [269] proposed a predictive framework for dislocation emission from $[2\bar{1}\bar{1}0]$ asymmetric tilt GBs by combining stress vector analysis with MD simulations (EAM_Liu potential). Their approach showed that both intrinsic GB stress states and external loading vectors control dislocation emission, providing a physics-based tool for designing GBs that promote or suppress specific deformation mechanisms.

7. Defect-defect interactions

Defect–defect interactions, including dislocation–twin, twin–twin, dislocation–precipitate, and boundary–precipitate interactions, in Mg and its alloys have been extensively studied using atomistic simulations. These investigations go beyond the capabilities of first-principles methods, due to the larger system sizes and longer timescales required. A fundamental understanding of these interactions is critical for revealing the synergistic effects of multiple defect types on the overall mechanical behavior of Mg alloys. A comprehensive review of dislocation–twin and twin–twin interactions has been provided by Yuan et al. [271]. Although a few additional studies have emerged in this rapidly evolving field [272–274], we refer readers to that review for detailed coverage of twin-related interactions. In this section, we instead focus on dislocation–precipitate and boundary–precipitate interactions, which play a pivotal role in precipitation hardening and microstructural evolution in Mg alloys (as illustrated in Fig. 8(a)).

7.1. Dislocation-precipitate

The interaction between dislocations and $Mg_{17}Al_{12}$ precipitates in Mg alloys has been extensively studied using atomistic simulations to understand their role in strengthening mechanisms. Liao et al. [275] investigated prismatic dislocation interactions with $Mg_{17}Al_{12}$ precipitates using MD simulations, revealing that prismatic dislocations can penetrate precipitates under sufficient applied stress. Building on this work, Liao et al. [276] examined basal dislocations interacting with precipitates using MD, showing that dislocations can glide through the matrix-precipitate interface without forming classical Orowan loops and the precipitate is only elastically sheared. Frequent cross-slip and jog formation were observed, particularly in the presence of smaller precipitates. Groh [277] employed MS simulations to model edge dislocation bypass of impenetrable $Mg_{17}Al_{12}$ particles. Successive dislocation interactions were found to transform initial shear loops into prismatic loops via cross-slip, thereby decreasing the required bypassing stress and altering the hardening response. Esteban-Manzanares et al. [278] studied the influence of interface strength and precipitate morphology using MD. Their findings indicated that strong matrix-precipitate interfaces favor Orowan looping, whereas weaker interfaces permit dislocation penetration. Furthermore, precipitates with lower aspect ratios enhanced the strengthening effect by increasing the frequency of dislocation-precipitate interactions. Vaid et al. [86] systematically assessed the interactions between basal dislocations and $Mg_{17}Al_{12}$ precipitates using atomistic simulations as shown in Fig. 8(b). In contrast to earlier find-

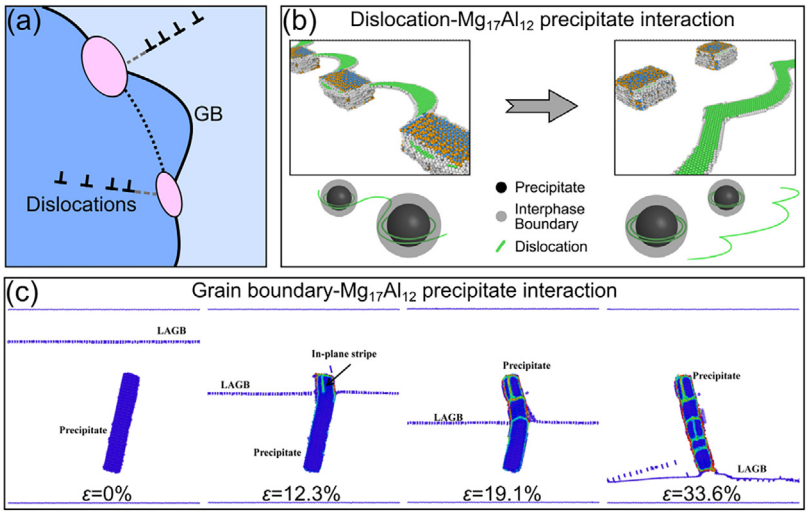

Fig. 8. Atomistic simulations of dislocation- and GB-precipitate interactions. (a) Schematics of dislocation- and GB-precipitate interactions in Mg alloys. (b) Atomistic simulations of interactions between dislocations and $Mg_{17}Al_{12}$ precipitate in Mg matrix revealed that dislocations bypass the precipitates by depositing dislocation segments into the disordered interphase boundary, rather than shearing the precipitate or forming Orowan loops in the surrounding matrix [86]. (c) MD simulations of interactions between a low-angle GB and $Mg_{17}Al_{12}$ precipitate with a rotation angle of 12° in the Mg matrix revealed that the precipitate was sheared by the GB [270]. Reprinted with permission from publishing houses.

ings, they observed that dislocations tend to be absorbed at the interface rather than shearing through the precipitate, with the size, shape, and spacing of precipitates playing a significant role in controlling the overall strengthening response.

Laves phases, which are common intermetallics in Mg alloys, have also been investigated through atomistic simulations to assess their strengthening behavior. Guénolé et al. [124] investigated the co-deformation behavior of a dual-phase Mg-C14 $CaMg_2$ using atomistic simulations combined with experiments. They demonstrated that plasticity can be transferred from the Mg matrix to the $CaMg_2$ Laves phase via direct or indirect slip transfer, depending on orientation, and highlighted interfacial sliding as a key deformation mechanism, consistent with experimental observations. Esteban-Manzanares et al. [279] performed atomistic simulations to analyze the interactions between edge basal dislocations and C14 $MgZn_2$ precipitates in Mg alloys. They found that dislocations initially bypass precipitates through Orowan looping and eventually shear them, with the shearing mechanism depending on precipitate size and temperature. Liu et al. [280] studied dislocation interactions with C15 $CaAl_2$ Laves phase particles in Mg-Al-Ca alloys through atomistic simulations. They observed shearing in small particles and cross-slip near larger ones, with strengthening arising from increased CRSS for larger particles, thereby contributing to improved plasticity.

Dislocation interactions with other metastable phases in Mg alloys have also been investigated. Huang et al. combined *in situ* TEM with MD simulations to study dislocation interactions with β''' precipitates in Mg-Nd alloys [281]. They found that metastable β''' precipitates are sheared directly by dislocations, whereas stable β_1 precipitates are bypassed via double cross-slip, contributing to increased strain hardening and ductility. Additionally, the strengthening effects of amorphous precipitates have been studied using MD simulations [282,283], revealing a range of interaction mechanisms, including dislocation pinning, cross-slip, and loop formation.

7.2. Boundary-precipitate

The interactions between GBs, particularly TBs, and $Mg_{17}Al_{12}$ precipitates have been investigated using atomistic simulations. Li and Mathaudhu [284] conducted MD simulations to examine the interaction between a $Mg_{17}Al_{12}$ precipitate and $\{10\bar{1}2\}$ TBs in Mg. They found that the precipitate could be fully engulfed by the twin without being sheared, and that the twinning was mediated by atomic shuffling rather than dislocations, resulting in zero shear strain. Wang and Li [285] performed atomistic simulations on the interaction between migrating $\{10\bar{1}2\}$ TBs and $Mg_{17}Al_{12}$ precipitates. They discovered that precipitate deflection occurs due to differential strain states and internal relaxation rather than twinning shear, offering new insights into twin-precipitate interactions. Fan et al. [286] investigated the effect of $Mg_{17}Al_{12}$ precipitate orientation on $\{10\bar{1}2\}$ twinning using MD, showing that parallel-oriented precipitates offer stronger resistance to twin propagation, and blocking effects decrease with increasing misorientation. Fan et al. [287] also analyzed how precipitate morphology affects $\{10\bar{1}2\}$ twinning in Mg alloys using MD. They found that TBs absorb $Mg_{17}Al_{12}$ precipitates without shearing them, leading to elastic deformation and rotation. Later, Fan and El-Awady [288] investigated the shape effect of $Mg_{17}Al_{12}$ precipitates (plate-, cube-, and rod-like) on TB migration using MD. They found that plate-like and cube-like precipitates exert similar and strong blocking effects on TBs, while the hardening effect of rod-like precipitates decreases as their aspect ratio increases. More recently, Fan and co-authors [289] explored the interaction of sheared plate-like $Mg_{17}Al_{12}$

precipitates with {11$\bar{2}$1} TBs in Mg alloys via MD. They proposed an analytical hardening model, showing that blocking effects depend on precipitate geometry, with larger and thicker precipitates providing stronger barriers to twinning. They also studied the interaction of low-angle GBs with $Mg_{17}Al_{12}$ precipitates via MD [270], finding that precipitates are sheared by boundaries with misorientation angles $\geq 9^\circ$ (see Fig. 8(c)). Additionally, they also explored how $Mg_{17}Al_{12}$ precipitates influence twin nucleation, propagation, and growth in Mg-Al alloys using MD [290]. Their findings suggest that while precipitates do not significantly affect twin nucleation, they act as obstacles during twin growth, exhibiting a clear size-dependent blocking effect, where larger precipitates are more effective in hindering twinning.

8. Future prospects

Despite significant advances in the atomic-scale modeling of defects in Mg and its alloys, several important challenges and opportunities remain open. These future directions span deeper mechanistic understanding and methodological developments.

8.1. Defect phase engineering

Defects can exist in multiple structurally and chemically distinct configurations, each stable within specific thermodynamic and kinetic constraints. These distinct defect states, often referred to as defect phases, represent localized equilibrium configurations whose physical properties vary smoothly with intensive control variables such as temperature, chemical potential, and external stress [82]. Analogous to conventional bulk phases, defect phases can coexist and transform, yet they remain spatially confined to the vicinity of the defect. The concept of defect phase engineering thus extends traditional thermodynamic phase engineering to the defect scale, integrating thermodynamics, chemistry, and mechanics into a unified framework [82]. By constructing and interpreting defect phase diagrams, which map the stability and transitions of these confined defect states, it becomes possible to predict and tailor how solute segregation, strain, or temperature control the structural and chemical complexity of defects.

A growing body of evidence suggests the presence of metastable defect phases in Mg alloys, such as dislocation- and GB-associated structures, which exhibit chemical and structural configurations distinct from the surrounding matrix [36,71,83]. These metastable configurations can have a significant influence on mechanical behavior, distinct from simple solute decoration or defect-associated thermodynamically stable phases, by mechanisms such as pinning dislocations or hindering GB motion. Despite their potential impact, a systematic investigation for identifying and predicting these defect phases is still lacking. Constructing defect phase diagrams that map stable and metastable defect structures and their energetics as a function of chemical potential would provide a valuable framework for alloy design [82]. Achieving this vision will require data-driven approaches that integrate high-precision atomic-scale calculations with advanced experimental characterization. In parallel, dynamic simulations are essential to develop deformation mechanism maps that account for the presence of defect phases and to establish mechanism–property relationships that can guide defect engineering strategies in Mg alloys.

8.2. Early-stage solute configurations

While solute enrichment behavior has been widely studied using atomic-scale modeling, the interactions between glissile dislocations or mobile GBs and early-stage solute configurations, such as short-range order clusters or metastable precipitates, remain poorly understood. These interactions are essential for elucidating the mechanisms of dislocation pinning and solute drag in Mg alloys. Further atomistic simulations are needed to elucidate how these transient solute structures influence defect mobility and mechanical response. Additionally, the structural evolution of both defects and solute configurations is often coupled under applied stress and temperature, resulting in complex feedback mechanisms that govern plastic deformation. A classical example is dynamic strain aging, where solute diffusion is coupled with dislocation motion, resulting in serrated flow behavior. Capturing these coupled dynamics is essential for developing predictive models of rate-dependent plasticity and microstructure evolution in Mg alloys.

8.3. Slip transmission at interphase boundaries

Classical MD simulations are widely used to study defect interactions but are constrained by nanosecond time scales and therefore high rates. In structurally complex intermetallics, such as TCP phases and $CaCu_5$-type phases [291–294], dislocation motion involving atomic shuffling or short-range diffusion often requires substantial thermal assistance. This implies that typical MD timescales may be insufficient to capture the full range of dislocation dynamics, particularly thermally activated slip mechanisms. As a result, the plastic deformation of these intermetallics in MD simulations may proceed through alternative athermal pathways occurring that require unrealistically high CRSS. Consequently, intermetallic precipitates are often observed as impenetrable in MD studies, which may not accurately reflect their behavior under experimental conditions. Likewise, observed slip transmission events in MD may not correspond to the most favorable or dominant mechanisms at experimental timescales. Therefore, careful consideration is required when interpreting MD simulation results and comparing them with experimental observations, particularly in the context of dislocation behavior in complex intermetallic systems. To address this, accelerated MD methods [295], such as hyperdynamics, parallel replica dynamics, or temperature-accelerated dynamics, will help access thermally activated pathways and yield more experimentally relevant predictions.

8.4. Machine learning interatomic potentials

Machine learning-based interatomic potentials have achieved remarkable accuracy, often approaching the fidelity of DFT, and have clearly outperformed classical empirical potentials in capturing bulk and defect energetics in Mg and its alloys, as illustrated in Fig. 2. However, their practical application in large-scale simulations remains significantly limited. The primary bottleneck is their high computational cost, typically two to three orders of magnitude more expensive than classical potentials, making them impractical for modeling extended system sizes and long time scales. Consequently, MLIPs are mostly employed in static calculations or for relatively small system sizes, restricting their broader impact on defect dynamics.

Recent developments on universal interatomic potentials, such as the graph atomic cluster expansion (GRACE) potential [296], represent a further evolution of the MLIP framework. These universal MLIPs are trained on a chemically diverse dataset and designed to be transferable across a wide range of compositions without retraining. This advancement opens the door to high-throughput exploration of chemical complexity in multicomponent Mg alloys, including high-entropy systems. With such universal MLIPs, it becomes feasible to simulate realistic chemical effects on precipitation, segregation, and defect–defect interactions, phenomena that are difficult to capture using DFT due to system size limitations or with classical interatomic potentials due to their restricted elemental coverage. These next-generation MLIPs mark a pivotal step toward data-driven alloy design, combining quantum-mechanics level accuracy with broader chemical and structural applicability.

9. Conclusions

Atomic-scale modeling has emerged as a powerful and indispensable tool for unraveling the complex behavior of crystallographic defects in Mg and its alloys. By providing fundamental insights into defect structures, energetics, and interactions across multiple length and time scales, these methods enable a deeper understanding of the mechanisms that govern phase stability, texture evolution, and plasticity in Mg-based materials. This review summarizes the current state of knowledge in atomic-scale modeling of major defect types, including solute distributions, dislocations, twinning, GBs, and defect–defect interactions, and highlights the role of various modeling techniques, ranging from first-principles calculations to large-scale atomistic simulations and hybrid approaches.

Recent developments in interatomic potentials, particularly machine-learning-based models, have significantly improved the fidelity of simulations, enabling increasingly realistic modeling of chemically complex systems. At the same time, growing evidence for metastable defect phases and solute configurations suggests new opportunities in defect engineering and alloy design for Mg alloys. These advancements underscore the evolving synergy between atomic-scale modeling, continuum-level approaches, and experimental observations. Looking ahead, integrating atomic-scale insights into multiscale frameworks and leveraging data-driven methodologies will be critical for accelerating the discovery and optimization of high-performance Mg alloys. By bridging fundamental defect physics with macroscopic materials behavior, atomic-scale modeling continues to play a central role in advancing our understanding and design of next-generation lightweight structural materials.

Declaration of competing interest

The authors declare the following financial interests/personal relationships which may be considered as potential competing interests:

Talal Al-Samman is an editorial board member for Journal of Magnesium and Alloys and was not involved in the editorial review or the decision to publish this article. All authors declare that there are no competing interests.

CRediT authorship contribution statement

Zhuocheng Xie: Writing – review & editing, Writing – original draft, Visualization, Project administration, Funding acquisition, Conceptualization. **Julien Guénolé:** Writing – review & editing, Funding acquisition, Conceptualization. **Hexin Wang:** Writing – review & editing. **Joé Petrazoller:** Writing – review & editing. **Fatim-Zahra Mouhib:** Writing – review & editing. **Antoine Guitton:** Writing – review & editing, Funding acquisition. **Thiebaud Richeton:** Writing – review & editing, Project administration, Funding acquisition. **Stéphane Berbenni:** Writing – review & editing, Funding acquisition. **Talal Al-Samman:** Writing – review & editing, Funding acquisition.

Acknowledgements

The authors acknowledge the financial support by the Deutsche Forschungsgemeinschaft (DFG) - Projektnummer 505716422 and the French National Research Agency (ANR) grants ANR22-CE92-0058-01 (SILA) and ANR-21-CE08-0001 (ATOUUM). Z.X. acknowledges financial support by the DFG through the projects A05 of the SFB1394 Structural and Chemical Atomic Complexity – From Defect Phase Diagrams to Material Properties, project ID 409476157. Z.X. acknowledges financial support funded by the DFG – Projektnummer 562592407 and 555365333.

References

[1] B.L. Mordike, T. Ebert, Materials Science and Engineering: A 302 (1) (2001) 37–45.
[2] T.M. Pollock, Science 328 (5981) (2010) 986–987.
[3] T. Li, J. Song, A. Zhang, G. You, Y. Yang, B. Jiang, X. Qin, C. Xu, F. Pan, Journal of Magnesium and Alloys 11 (11) (2023) 4166–4180.
[4] B. Liu, J. Yang, X. Zhang, Q. Yang, J. Zhang, X. Li, Journal of Magnesium and Alloys 11 (1) (2023) 15–47.

[5] J. Bai, Y. Yang, C. Wen, J. Chen, G. Zhou, B. Jiang, X. Peng, F. Pan, Journal of Magnesium and Alloys 11 (10) (2023) 3609–3619.
[6] L. Liu, X. Chen, F. Pan, Journal of Magnesium and Alloys 9 (6) (2021) 1906–1921.
[7] D. Bairagi, S. Mandal, Journal of Magnesium and Alloys 10 (3) (2022) 627–669.
[8] S. Bai, B. Jiang, W. He, J. Song, K. Li, Y. Yang, J. Zheng, G. Huang, D. Zhang, F. Pan, Journal of Materials Research and Technology 33 (2024) 4908–4937.
[9] Q. Chen, R. Chen, J. Su, Q. He, B. Tan, C. Xu, X. Huang, Q. Dai, J. Lu, Journal of Magnesium and Alloys 10 (9) (2022) 2384–2397.
[10] Z.-Z. Jin, M. Zha, S.-Q. Wang, S.-C. Wang, C. Wang, H.-L. Jia, H.-Y. Wang, Journal of Magnesium and Alloys 10 (5) (2022) 1191–1206.
[11] M.-T. Pérez-Prado, J. Bohlen, S. Yi, D. Letzig, T. Al-Samman, J. Robson, M. Barnett, W. Poole, C. Mendis, S. Agnew, et al., JOM 72 (7) (2020) 2561–2567.
[12] D. Hull, D.J. Bacon, Introduction to Dislocations, vol. 37, Elsevier, 2011.
[13] J.W. Christian, S. Mahajan, Progress in Materials Science 39 (1-2) (1995) 1–157.
[14] G. Gottstein, S. Korte-Kerzel, Materialwissenschaft und Werkstofftechnik: Physikalische Grundlagen, Springer-Verlag, 2025.
[15] M.R. Barnett, Twinning and its role in wrought magnesium alloys, in: Advances in Wrought Magnesium Alloys, Elsevier, 2012, pp. 105–143.
[16] J.-F. Nie, Metallurgical and Materials Transactions A 43 (11) (2012) 3891–3939.
[17] J. Hirsch, T. Al-Samman, Acta Materialia 61 (3) (2013) 818–843.
[18] N. Li, C. Wang, M.A. Monclús, L. Yang, J.M. Molina-Aldareguia, Acta Materialia 221 (2021) 117374.
[19] H. Ovri, J. Markmann, J. Barthel, M. Kruth, H. Dieringa, E.T. Lilleodden, Acta Materialia 244 (2023) 118550.
[20] R. Pei, Y. Zou, M. Zubair, D. Wei, T. Al-Samman, Acta Materialia 233 (2022) 117990.
[21] J. Wang, J.M. Molina-Aldareguía, J. LLorca, Acta Materialia 188 (2020) 215–227.
[22] Z. Wu, R. Ahmad, B. Yin, S. Sandlöbes, W.A. Curtin, Science 359 (6374) (2018) 447–452.
[23] P. Giannozzi, S. Baroni, N. Bonini, M. Calandra, R. Car, C. Cavazzoni, D. Ceresoli, G.L. Chiarotti, M. Cococcioni, I. Dabo, A. Dal Corso, S. de Gironcoli, S. Fabris, G. Fratesi, R. Gebauer, U. Gerstmann, C. Gougoussis, A. Kokalj, M. Lazzeri, L. Martin-Samos, N. Marzari, F. Mauri, R. Mazzarello, S. Paolini, A. Pasquarello, L. Paulatto, C. Sbraccia, S. Scandolo, G. Sclauzero, A.P. Seitsonen, A. Smogunov, P. Umari, R.M. Wentzcovitch, Journal of Physics: Condensed Matter 21 (39) (2009). 395502 (19pp)
[24] G. Kresse, J. Furthmüller, Physical Review B 54 (16) (1996) 11169.
[25] A.P. Thompson, H.M. Aktulga, R. Berger, D.S. Bolintineanu, W.M. Brown, P.S. Crozier, P.J. In't Veld, A. Kohlmeyer, S.G. Moore, T.D. Nguyen, et al., Computer Physics Communications 271 (2022) 108171.
[26] X.-Y. Liu, P.P. Ohotnicky, J.B. Adams, C.L. Rohrer, R.W.Jr Hyland, Surface Science 373 (2-3) (1997) 357–370.
[27] Y.-M. Kim, N.J. Kim, B.-J. Lee, Calphad 33 (4) (2009) 650–657.
[28] M.S. Nitol, S. Mun, D.E. Dickel, C.D. Barrett, Philosophical Magazine 102 (8) (2022) 651–673.
[29] M. Li, X. Tian, W. Jiang, Q. Wang, H. Fan, Journal of the Mechanics and Physics of Solids 173 (2023) 105238.
[30] C. Liu, F. Roters, D. Raabe, Acta Materialia 242 (2023) 118444.
[31] M.P. Allen, D.J. Tildesley, Computer Simulation of Liquids, Oxford University Press, 2017.
[32] F. Giustino, Materials Modelling Using Density Functional Theory: Properties and Predictions, Oxford University Press, 2014.
[33] D.S. Sholl, J.A. Steckel, Density Functional Theory: A Practical Introduction, John Wiley & Sons, 2022.
[34] E.B. Tadmor, R.E. Miller, Modeling Materials: Continuum, Atomistic and Multiscale Techniques, Cambridge University Press, 2011.
[35] L. Huber, J. Rottler, M. Militzer, Acta Materialia 80 (2014) 194–204.
[36] X. Zhou, P. Mathews, B. Berkels, W. Delis, S. Saood, A. Shamseldeen Ali Alhassan, P. Keuter, J.M. Schneider, S. Korte-Kerzel, S. Sandlöbes-Haut, et al., Advanced Materials 37 (3) (2025) 2402191.
[37] Z. Pei, R. Li, J.-F. Nie, J.R. Morris, Materials & Design 165 (2019) 107574.
[38] Z. Pei, X. Zhang, T. Hickel, M. Friák, S. Sandlöbes, B. Dutta, J. Neugebauer, NPJ Computational Materials 3 (1) (2017) 6.
[39] G. Kresse, D. Joubert, Physical Review b 59 (3) (1999) 1758.
[40] G. Prandini, A. Marrazzo, I.E. Castelli, N. Mounet, N. Marzari, npj Computational Materials 4 (1) (2018) 72.
[41] C.S. Barrett, T.B. Massalski, Structure of Metals, Crystallographic Methods, Principles, and Data, 3d ed., Rev, PergamonPress, New York, 1980, pp. 256–259.
[42] G. Simmons, Journal of the Graduate Research Center 34 (1971) 140.
[43] Y. Wang, L.-Q. Chen, Z.-K. Liu, S.N. Mathaudhu, Scripta Materialia 62 (9) (2010) 646–649.
[44] B. Yin, Z. Wu, W.A. Curtin, Acta Materialia 123 (2017) 223–234.
[45] M.I. Mendelev, M. Asta, M.J. Rahman, J.J. Hoyt, Philosophical Magazine 89 (34-36) (2009) 3269–3285.
[46] S.R. Wilson, M.I. Mendelev, The Journal of Chemical Physics 144 (14) (2016).
[47] B. Jelinek, J. Houze, S. Kim, M.F. Horstemeyer, M.I. Baskes, S.-G. Kim, Physical Review B-Condensed Matter and Materials Physics 75 (5) (2007) 054106.
[48] Z. Wu, M.F. Francis, W.A. Curtin, Modelling and Simulation in Materials Science and Engineering 23 (1) (2015) 015004.
[49] E. Ibrahim, Y. Lysogorskiy, M. Mrovec, R. Drautz, Physical Review Materials 7 (11) (2023) 113801.
[50] M. Poul, L. Huber, E. Bitzek, J. Neugebauer, Physical Review B 107 (10) (2023) 104103.
[51] M. Stricker, B. Yin, E. Mak, W.A. Curtin, Physical Review Materials 4 (10) (2020) 103602.
[52] R. Jacobs, D. Morgan, S. Attarian, J. Meng, C. Shen, Z. Wu, C.Y. Xie, J.H. Yang, N. Artrith, B. Blaiszik, et al., Current Opinion in Solid State and Materials Science 35 (2025) 101214.
[53] M.H. Müser, S.V. Sukhomlinov, L. Pastewka, Advances in Physics: X 8 (1) (2023) 2093129.
[54] Y.-W. Zhang, V. Sorkin, Z.H. Aitken, A. Politano, J. Behler, A.P. Thompson, T.W. Ko, S.P. Ong, O. Chalykh, D. Korogod, et al., Modelling and Simulation in Materials Science and Engineering 33 (2) (2025) 023301.
[55] M.S. Daw, M.I. Baskes, Physical review B 29 (12) (1984) 6443.
[56] M. Freund, Z. Xie, M. Kolb, P.-L. Sun, M. Hans, J.M. Wheeler, S. Korte-Kerzel, Materials & Design 255 (2025) 114151.
[57] H. Wang, J. Guénolé, S. Korte-Kerzel, T. Al-Samman, Z. Xie, Computational Materials Science 240 (2024) 113025.
[58] M.I. Baskes, Physical Review B 46 (5) (1992) 2727.
[59] J. Behler, M. Parrinello, Physical Review Letters 98 (14) (2007) 146401.
[60] R. Drautz, Physical Review B 99 (1) (2019) 014104.
[61] A.V. Shapeev, Multiscale Modeling & Simulation 14 (3) (2016) 1153–1173.
[62] J. Guénolé, W.G. Nöhring, A. Vaid, F. Houllé, Z. Xie, A. Prakash, E. Bitzek, Computational Materials Science 175 (2020) 109584.
[63] V. Bulatov, W. Cai, Computer Simulations of Dislocations, vol. 3, Oxford University Press, 2006.
[64] G. Henkelman, H. Jónsson, The Journal of Chemical Physics 113 (22) (2000) 9978–9985.
[65] G. Henkelman, B.P. Uberuaga, H. Jónsson, The Journal of Chemical Physics 113 (22) (2000) 9901–9904.
[66] A. Warshel, M. Levitt, Journal of Molecular Biology 103 (2) (1976) 227–249.
[67] L. Huber, B. Grabowski, M. Militzer, J. Neugebauer, J. Rottler, Acta Materialia 132 (2017) 138–148.
[68] M. Wagih, C.A. Schuh, Physical Review Letters 129 (4) (2022) 046102.

[69] B. Sadigh, P. Erhart, A. Stukowski, A. Caro, E. Martinez, L. Zepeda-Ruiz, Physical Review B–Condensed Matter and Materials Physics 85 (18) (2012) 184203.
[70] S. Zhang, Z. Xie, P. Keuter, S. Saood, L. Abdellaoui, X. Zhou, N. Cautaerts, B. Breitbach, S. Aliramaji, S. Korte-Kerzel, et al., Nanoscale 14 (48) (2022) 18192–18199.
[71] A. Ganguly, H. Wang, J. Guénolé, A. Prakash, S. Korte-Kerzel, T. Al-Samman, Z. Xie, Acta Materialia 283 (2025) 120556.
[72] P. Yi, T.T. Sasaki, S.E. Prameela, T.P. Weihs, M.L. Falk, Acta Materialia 249 (2023) 118805.
[73] J.D. Honeycutt, H.C. Andersen, Journal of Physical Chemistry 91 (19) (1987) 4950–4963.
[74] P.M. Larsen, S. Schmidt, J. Schiøtz, Modelling and Simulation in Materials Science and Engineering 24 (5) (2016) 055007.
[75] G.J. Ackland, A.P. Jones, Physical Review B-Condensed Matter and Materials Physics 73 (5) (2006) 054104.
[76] A. Stukowski, K. Albe, Modelling and Simulation in Materials Science and Engineering 18 (8) (2010) 085001.
[77] C.L. Kelchner, S.J. Plimpton, J.C. Hamilton, Physical review B 58 (17) (1998) 11085.
[78] F. Shimizu, S. Ogata, J. Li, Materials Transactions 48 (11) (2007) 2923–2927.
[79] G. Voronoi, Journal für die reine und Angewandte Mathematik (Crelles Journal) 1908 (133) (1908) 97–102.
[80] J.H. Irving, J.G. Kirkwood, The Journal of Chemical Physics 18 (6) (1950) 817–829.
[81] Z. Xie, D. Chauraud, E. Bitzek, S. Korte-Kerzel, J. Guénolé, Journal of Materials Research 36 (10) (2021) 2010–2024.
[82] S. Korte-Kerzel, T. Hickel, L. Huber, D. Raabe, S. Sandlöbes-Haut, M. Todorova, J. Neugebauer, International Materials Reviews 67 (1) (2022) 89–117.
[83] Z. Yang, L. Zhang, M.F. Chisholm, X. Zhou, H. Ye, S.J. Pennycook, Nature Communications 9 (1) (2018) 809.
[84] J.F. Nie, N.C. Wilson, Y.M. Zhu, Z. Xu, Acta Materialia 106 (2016) 260–271.
[85] A.R. Natarajan, E.L.S. Solomon, B. Puchala, E.A. Marquis, A. Van der Ven, Acta Materialia 108 (2016) 367–379.
[86] A. Vaid, J. Guénolé, A. Prakash, S. Korte-Kerzel, E. Bitzek, Materialia 7 (2019) 100355.
[87] S. Sandlöbes, M. Friák, S. Zaefferer, A. Dick, S.-b. Yi, D. Letzig, Z.-r. Pei, L.-F. Zhu, J. Neugebauer, D. Raabe, Acta Materialia 60 (6-7) (2012) 3011–3021.
[88] T. Chen, Y. Yuan, X. Mi, J. Wu, A. Tang, J. Wang, N. Moelans, F. Pan, journal of Materials Research and Technology 21 (2022) 4512–4525.
[89] G. Liu, J. Zhang, Y. Dou, Computational Materials Science 103 (2015) 97–104.
[90] J.E. Saal, C. Wolverton, Acta Materialia 60 (13-14) (2012) 5151–5159.
[91] D. Shin, C. Wolverton, Acta Materialia 58 (2) (2010) 531–540.
[92] F. Mouhib, Z. Xie, A. Atila, J. Guénolé, S. Korte-Kerzel, T. Al-Samman, Acta Materialia 266 (2024) 119677.
[93] L. Huber, I. Elfimov, J. Rottler, M. Militzer, Physical Review B-Condensed Matter and Materials Physics 85 (14) (2012) 144301.
[94] B.-C. Zhou, S.-L. Shang, Y. Wang, Z.-K. Liu, Acta Materialia 103 (2016) 573–586.
[95] R. Agarwal, D.R. Trinkle, Physical Review Letters 118 (10) (2017) 105901.
[96] R. Agarwal, D.R. Trinkle, Acta Materialia 150 (2018) 339–350.
[97] G. Nandipati, N. Govind, A. Andersen, A. Rohatgi, Journal of Physics: Condensed Matter 28 (15) (2016) 155001.
[98] H. Kimizuka, S. Ogata, Materials Research Letters 1 (4) (2013) 213–219.
[99] J.E. Saal, C. Wolverton, Scripta Materialia 67 (10) (2012) 798–801.
[100] A.R. Natarajan, A. Van der Ven, Acta Materialia 124 (2017) 620–632.
[101] A.R. Natarajan, A. Van der Ven, Physical Review B 95 (21) (2017) 214107.
[102] D. Cheng, E.R. Hoglund, K. Wang, J.M. Howe, S.R. Agnew, B.-C. Zhou, Scripta Materialia 216 (2022) 114744.
[103] H. Jiang, S.-X. Li, L.-L. Hao, W.-J. Li, Z.-Q. Han, L.-X. Lv, L. Zhen, Journal of Magnesium and Alloys 13 (3) (2025) 1078–1087.
[104] H. Liao, H. Kimizuka, A. Ishii, J.-P. Du, S. Ogata, Scripta Materialia 210 (2022) 114480.
[105] J. Bai, X. Pang, X. Meng, H. Xie, H. Pan, Y. Ren, M. Jiang, G. Qin, Journal of Materials Science & Technology 36 (2020) 167–175.
[106] D. Cheng, K. Wang, B.-C. Zhou, Acta Materialia 242 (2023) 118443.
[107] D. Choudhuri, Computational Materials Science 187 (2021) 110111.
[108] Y. Guo, B. Liu, W. Xie, Q. Luo, Q. Li, Scripta Materialia 193 (2021) 127–131.
[109] H. Liu, Y.M. Zhu, N.C. Wilson, J.F. Nie, Acta Materialia 133 (2017) 408–426.
[110] S. Liu, G. Esteban-Manzanares, J. LLorca, Physical Review Materials 4 (9) (2020) 093609.
[111] Y.X. Liu, H. Liu, Y.M. Zhu, N.C. Wilson, J.F. Nie, Computational Materials Science 170 (2019) 109126.
[112] K. Matsubara, H. Kimizuka, S. Ogata, Journal of Alloys and Compounds 657 (2016) 662–670.
[113] X.-S. Niu, M. Lv, Y.-P. Feng, Y.-J. Wang, X.-H. Shao, X.-L. Ma, Acta Materialia 286 (2025) 120746.
[114] E.L.S. Solomon, A.R. Natarajan, A.M. Roy, V. Sundararaghavan, A. Van der Ven, E.A. Marquis, Acta Materialia 166 (2019) 148–157.
[115] D. Wang, M. Amsler, V.I. Hegde, J.E. Saal, A. Issa, B.-C. Zhou, X. Zeng, C. Wolverton, Acta Materialia 158 (2018) 65–78.
[116] K. Wang, D. Cheng, C.-L. Fu, B.-C. Zhou, Physical Review Materials 4 (1) (2020) 013606.
[117] T. Wang, F. Liu, Acta Materialia 254 (2023) 119011.
[118] Q. Zhu, Y. Li, H. Zhang, X. Qi, X. Zeng, Materials Letters 305 (2021) 130857.
[119] A. Issa, J.E. Saal, C. Wolverton, Acta Materialia 65 (2014) 240–250.
[120] A. Issa, J.E. Saal, C. Wolverton, Acta Materialia 83 (2015) 75–83.
[121] Q. Shi, A.R. Natarajan, A. Van der Ven, J. Allison, Materials Research Letters 11 (3) (2023) 222–230.
[122] Z.-M. Hua, S.-L. Wu, M. Zha, Y. Zhu, Z. Hu, P. Chen, X.-Y. Xu, S. Li, C. Wang, S.-B. Jin, U. Ramamurty, H.-Y. Wang, Acta Materialia 301 (2025) 121572.
[123] F.X. Wang, B. Li, Journal of Magnesium and Alloys 6 (4) (2018) 375–383.
[124] J. Guénolé, M. Zubair, S. Roy, Z. Xie, M. Lipińska-Chwałek, S. Sandlöbes-Haut, S. Korte-Kerzel, Materials & Design 202 (2021) 109572.
[125] D. Rodney, L. Ventelon, E. Clouet, L. Pizzagalli, F. Willaime, Acta Materialia 124 (2017) 633–659.
[126] J.A. Yasi, T. Nogaret, D.R. Trinkle, Y. Qi, L.G. Hector, W.A. Curtin, Modelling and Simulation in Materials Science and Engineering 17 (5) (2009) 055012.
[127] M. Stricker, W.A. Curtin, The Journal of Physical Chemistry C 124 (49) (2020) 27230–27240.
[128] J. Jeong, Z. Xie, M. Alfreider, S. Korte-Kerzel, D. Kiener, J. Guénolé, S.H. Oh, Acta Materialia (2025) 121261.
[129] Z. Pei, D. Ma, M. Friák, B. Svendsen, D. Raabe, J. Neugebauer, Physical Review B 92 (6) (2015) 064107.
[130] I. Shin, E.A. Carter, Modelling and Simulation in Materials Science and Engineering 20 (1) (2011) 015006.
[131] I. Shin, E.A. Carter, International Journal of Plasticity 60 (2014) 58–70.
[132] D. Qiu, P. Zhao, D.R. Trinkle, Y. Wang, Materials Research Letters 9 (3) (2021) 134–140.
[133] Y. Dan, D.R. Trinkle, Materials Research Letters 10 (6) (2022) 360–368.
[134] M. Uranagase, R. Matsumoto, Physical Review B 89 (22) (2014) 224103.
[135] M. Itakura, H. Kaburaki, M. Yamaguchi, T. Tsuru, Modelling and Simulation in Materials Science and Engineering 23 (6) (2015) 065002.
[136] X. Liu, M.R. Niazi, T. Liu, B. Yin, W.A. Curtin, Acta Materialia 243 (2023) 118490.
[137] X. Liu, W.A. Curtin, Acta Materialia 262 (2024) 119402.
[138] B. Li, E. Ma, Philosophical Magazine 89 (14) (2009) 1223–1235.

[139] T. Nogaret, W.A. Curtin, J.A. Yasi, L.G.Jr Hector, D.R. Trinkle, Acta Materialia 58 (13) (2010) 4332–4343.
[140] M. Ghazisaeidi, L.G.Jr Hector, W.A. Curtin, Scripta Materialia 75 (2014) 42–45.
[141] K. Srivastava, S.I. Rao, J.A. El-Awady, Acta Materialia 161 (2018) 182–193.
[142] Y. Sun, Z. Ma, H. Chu, Scripta Materialia 255 (2025) 116370.
[143] H. Fan, J.A. El-Awady, Materials Science and Engineering: A 644 (2015) 318–324.
[144] Z. Ding, W. Liu, H. Sun, S. Li, D. Zhang, Y. Zhao, E.J. Lavernia, Y. Zhu, Acta Materialia 146 (2018) 265–272.
[145] A. Kumar, B.M. Morrow, R.J. McCabe, I.J. Beyerlein, Materials Science and Engineering: A 695 (2017) 270–278.
[146] Z. Li, C. Xu, X. Tian, W. Jiang, Q. Wang, H. Fan, Journal of Magnesium and Alloys 13 (7) (2025) 3198–3208.
[147] Q. Yu, L. Qi, R.K. Mishra, J. Li, A.M. Minor, Proceedings of the National Academy of Sciences 110 (33) (2013) 13289–13293.
[148] B.-Y. Liu, F. Liu, N. Yang, X.-B. Zhai, L. Zhang, Y. Yang, B. Li, J. Li, E. Ma, J.-F. Nie, et al., Science 365 (6448) (2019) 73–75.
[149] R. Ahmad, Z. Wu, W.A. Curtin, Acta Materialia 183 (2020) 228–241.
[150] Z. Wu, W.A. Curtin, Nature 526 (7571) (2015) 62–67.
[151] Z. Wu, W.A. Curtin, Scripta Materialia 116 (2016) 104–107.
[152] Z. Wu, B. Yin, W.A. Curtin, Acta Materialia 119 (2016) 203–217.
[153] Y. Yang, F. Liu, K. Chen, B. Liu, Z. Shan, B. Li, Journal of Magnesium and Alloys 11 (12) (2023) 4498–4512.
[154] R. Matsumoto, S.T. Oyinbo, D. Matsunaka, Scripta Materialia 252 (2024) 116235.
[155] Y. Tang, J.A. El-Awady, Acta Materialia 71 (2014) 319–332.
[156] Z. Wu, W.A. Curtin, Proceedings of the National Academy of Sciences 113 (40) (2016) 11137–11142.
[157] D. Buey, M. Ghazisaeidi, Scripta Materialia 117 (2016) 51–54.
[158] M. Itakura, H. Kaburaki, M. Yamaguchi, T. Tsuru, Physical Review Letters 116 (22) (2016) 225501.
[159] J. Zhang, Y. Zhang, J.A. El-Awady, Y. Tang, Scripta Materialia 156 (2018) 19–22.
[160] T. Liu, B. Yin, Acta Materialia 270 (2024) 119864.
[161] A. Datta, U.V. Waghmare, U. Ramamurty, Acta Materialia 56 (11) (2008) 2531–2539.
[162] J.A. Yasi, L.G.Jr Hector, D.R. Trinkle, Acta Materialia 58 (17) (2010) 5704–5713.
[163] B. Yin, Z. Wu, W.A. Curtin, Acta Materialia 136 (2017) 249–261.
[164] A. Tehranchi, B. Yin, W.A. Curtin, Acta Materialia 151 (2018) 56–66.
[165] D. Buey, L.G.Jr Hector, M. Ghazisaeidi, Acta Materialia 147 (2018) 1–9.
[166] C. Fang, J. Zhang, F. Pan, Journal of Alloys and Compounds 785 (2019) 911–917.
[167] M.R. Fellinger, L.G.Jr Hector, D.R. Trinkle, Physical Review Materials 6 (1) (2022) 013607.
[168] M.R. Niazi, W.A. Curtin, Modelling and Simulation in Materials Science and Engineering 32 (6) (2024) 065007.
[169] K.-H. Kim, J.B. Jeon, N.J. Kim, B.-J. Lee, Scripta Materialia 108 (2015) 104–108.
[170] K.-H. Kim, J.H. Hwang, H.-S. Jang, J.B. Jeon, N.J. Kim, B.-J. Lee, Materials Science and Engineering: A 715 (2018) 266–275.
[171] H.-S. Jang, B.-J. Lee, Scripta Materialia 160 (2019) 39–43.
[172] H.-S. Jang, J.-K. Lee, A.J.S.F. Tapia, N.J. Kim, B.-J. Lee, Journal of Magnesium and Alloys 10 (2) (2022) 585–597.
[173] J.-K. Lee, B.-J. Lee, Metallurgical and Materials Transactions A 52 (3) (2021) 964–974.
[174] J.A. Yasi, L.G. Jr Hector, D.R. Trinkle, Acta materialia 59 (14) (2011) 5652–5660.
[175] J.A. Yasi, L.G.Jr Hector, D.R. Trinkle, Acta Materialia 60 (5) (2012) 2350–2358.
[176] R. Ahmad, B. Yin, Z. Wu, W.A. Curtin, Acta Materialia 172 (2019) 161–184.
[177] J. Brodie, M. Ghazisaeidi, Scripta Materialia 224 (2023) 115075.
[178] R. Ahmad, Z. Wu, S. Groh, W.A. Curtin, Scripta Materialia 155 (2018) 114–118.
[179] R. Ahmad, S. Groh, M. Ghazisaeidi, W.A. Curtin, Modelling and Simulation in Materials Science and Engineering 26 (6) (2018) 065010.
[180] D. Utt, A. Stukowski, M. Ghazisaeidi, Scripta Materialia 182 (2020) 53–56.
[181] D.F. Shi, A. Ma, M.T. Pérez-Prado, C.M. Cepeda-Jiménez, Acta Materialia 244 (2023) 118555.
[182] D.E. Dickel, M.I. Baskes, I. Aslam, C.D. Barrett, Modelling and simulation in materials science and engineering 26 (4) (2018) 045010.
[183] A. Ishii, J. Li, S. Ogata, International Journal of Plasticity 82 (2016) 32–43.
[184] L. Jiang, M. Gong, J. Wang, Z. Pan, X. Wang, D. Zhang, Y.M. Wang, J. Ciston, A.M. Minor, M. Xu, et al., Nature Communications 13 (1) (2022) 20.
[185] X. Liao, J. Wang, J. Nie, Y. Jiang, P. Wu, Mrs Bulletin 41 (4) (2016) 314–319.
[186] M. Gong, G. Liu, J. Wang, L. Capolungo, C.N. Tomé, Acta Materialia 155 (2018) 187–198.
[187] Y. Liu, P.Z. Tang, M.Y. Gong, R.J. McCabe, J. Wang, C.N. Tomé, Nature Communications 10 (1) (2019) 3308.
[188] J. Wang, J.P. Hirth, C.N. Tomé, Acta Materialia 57 (18) (2009) 5521–5530.
[189] J. Wang, S.K. Yadav, J.P. Hirth, C.N. Tomé, I.J. Beyerlein, Materials Research Letters 1 (3) (2013) 126–132.
[190] G.-D. Sim, G. Kim, S. Lavenstein, M.H. Hamza, H. Fan, J.A. El-Awady, Acta Materialia 144 (2018) 11–20.
[191] J. Wang, R.G. Hoagland, J.P. Hirth, L. Capolungo, I.J. Beyerlein, C.N. Tomé, Scripta Materialia 61 (9) (2009) 903–906.
[192] J. Wang, L. Liu, C.N. Tomé, S.X. Mao, S.K. Gong, Materials Research Letters 1 (2) (2013) 81–88.
[193] J. Wang, I.J. Beyerlein, C.N. Tomé, Scripta Materialia 63 (7) (2010) 741–746.
[194] I.J. Beyerlein, R.J. McCabe, C.N. Tomé, Journal of the Mechanics and Physics of Solids 59 (5) (2011) 988–1003.
[195] Q. Yu, L. Qi, K. Chen, R.K. Mishra, J. Li, A.M. Minor, Nano letters 12 (2) (2012) 887–892.
[196] X.-Y. Li, Y.-F. Guo, Y. Mao, X.-Z. Tang, International Journal of Plasticity 158 (2022) 103437.
[197] Y. Wang, B. Li, Y. Liao, Acta Materialia 282 (2025) 120480.
[198] J. Xiao, J. Gao, S. Li, R. Wang, C. Deng, Y. Zhu, Z. Wu, Acta Materialia 285 (2025) 120648.
[199] B. Li, E. Ma, Physical Review Letters 103 (3) (2009) 035503.
[200] B. Li, E. Ma, Physical Review Letters 104 (2010) 029604.
[201] A. Serra, D.J. Bacon, R.C. Pond, Physical Review Letters 104 (2010) 029603.
[202] B.-Y. Liu, J. Wang, B. Li, L. Lu, X.-Y. Zhang, Z.-W. Shan, J. Li, C.-L. Jia, J. Sun, E. Ma, Nature Communications 5 (1) (2014) 3297.
[203] X. Wan, J. Zhang, X. Mo, F. Pan, Journal of Magnesium and Alloys 7 (3) (2019) 474–486.
[204] I.J. Beyerlein, C.N. Tomé, Proceedings of the Royal Society A: Mathematical, Physical and Engineering Sciences 466 (2121) (2010) 2517–2544.
[205] G. Proust, C.N. Tomé, G.C. Kaschner, Acta Materialia 55 (6) (2007) 2137–2148.
[206] P.-A. Juan, S. Berbenni, M.R. Barnett, C.N. Tomé, L. Capolungo, International Journal of Plasticity 60 (2014) 182–196.
[207] P.-A. Juan, S. Berbenni, L. Capolungo, Acta Materialia 60 (2) (2012) 476–486.
[208] M. Gong, J. Graham, V. Taupin, L. Capolungo, Acta Materialia 208 (2021) 116603.
[209] D.E. Spearot, V. Taupin, K. Dang, L. Capolungo, Mechanics of Materials 143 (2020) 103314.
[210] K. Dang, J. Graham, R.J. McCabe, V. Taupin, C.N. Tomé, L. Capolungo, Materialia 20 (2021) 101247.
[211] M.A. Kumar, K. Dang, V. Taupin, R.J. Mccabe, C.N. Tomé, L. Capolungo, Materialia 23 (2022) 101437.

[212] H. Chen, C. Chen, J. Song, S. Yue, Journal of Magnesium and Alloys 12 (12) (2024) 4923–4936.
[213] P. Chen, B. Li, Journal of Magnesium and Alloys 13 (2) (2025) 681–696.
[214] J.P. Hadorn, K. Hantzsche, S. Yi, J. Bohlen, D. Letzig, J.A. Wollmershauser, S.R. Agnew, Metallurgical and Materials Transactions A 43 (2012) 1347–1362.
[215] J.F. Nie, Y.M. Zhu, J.Z. Liu, X.-Y. Fang, Science 340 (6135) (2013) 957–960.
[216] X. Wang, Y. Hu, K. Yu, S. Mahajan, I.J. Beyerlein, E.J. Lavernia, T.J. Rupert, J.M. Schoenung, Scripta Materialia 209 (2022) 114375.
[217] Z. Xie, A. Atila, J. Guénolé, S. Korte-Kerzel, T. Al-Samman, U. Kerzel, Journal of Magnesium and Alloys (2025).
[218] Z. Xing, H. Fan, C. Xu, G. Kang, Acta Mechanica Sinica 40 (8) (2024) 123448.
[219] A. Kumar, J. Wang, C.N. Tomé, Acta Materialia 85 (2015) 144–154.
[220] H. Zhu, S. Liu, Z. Liu, D. Li, Computational Materials Science 152 (2018) 113–117.
[221] N.J. Lane, S.I. Simak, A.S. Mikhaylushkin, I.A. Abrikosov, L. Hultman, M.W. Barsoum, Physical Review B-Condensed Matter and Materials Physics 84 (18) (2011) 184101.
[222] Q. Zeng, M. Gong, H. Ma, Y. Shen, J.-f. Nie, J. Wang, Y. Liu, Journal of Magnesium and Alloys 13 (2) (2025) 626–639.
[223] X. Zhao, H. Chen, N. Wilson, Q. Liu, J.-F. Nie, Nature Communications 10 (1) (2019) 3243.
[224] X.F. Chen, L.R. Xiao, Z.G. Ding, W. Liu, Y.T. Zhu, X.L. Wu, Scripta Materialia 178 (2020) 193–197.
[225] H. Xie, H. Pan, J. Bai, D. Xie, P. Yang, S. Li, J. Jin, Q. Huang, Y. Ren, G. Qin, Nano Letters 21 (22) (2021) 9642–9650.
[226] C. He, Z. Li, D. Kong, X. Zhao, H. Chen, J.-F. Nie, Scripta Materialia 191 (2021) 62–66.
[227] C. He, Z. Li, H. Chen, N. Wilson, J.-F. Nie, Nature Communications 12 (1) (2021) 722.
[228] Q. Yang, S. Lv, P. Chen, Z. Xie, S. Zhou, X. Qiu, Journal of Magnesium and Alloys 13 (2) (2025) 583–591.
[229] D. Shi, Z. Lu, Y. Fan, Y. Liu, X. Zeng, L. Wang, Journal of Magnesium and Alloys 13 (6) (2025) 2670–2679.
[230] J. Zhang, Y. Dou, Y. Zheng, Scripta Materialia 80 (2014) 17–20.
[231] H. Chen, J. Song, Journal of Applied Physics 132 (22) (2022) 225102.
[232] H. Ma, M. Liu, W. Chen, C. Wang, X.-Q. Chen, J. Dong, W. Ke, Physical Review Materials 3 (5) (2019) 053806.
[233] Z. Huang, J.-F. Nie, Acta Materialia 214 (2021) 117009.
[234] D.E. Spearot, L. Capolungo, C.N. Tomé, Physical Review Materials 3 (5) (2019) 053606.
[235] P. Chen, F. Wang, B. Li, Computational Materials Science 164 (2019) 186–194.
[236] K. Yu, X. Wang, S. Mahajan, T.J. Rupert, I.J. Beyerlein, P. Cao, J.M. Schoenung, E.J. Lavernia, Computational Materials Science 246 (2025) 113414.
[237] Z. Li, H. Chen, J.-F. Nie, Scripta Materialia 236 (2023) 115671.
[238] B. Ge, M. Yang, Q. Zu, J. Guo, Y. Tian, Q. Peng, Acta Materialia 201 (2020) 477–487.
[239] J. Tang, X. Tian, W. Jiang, Q. Wang, D. Wei, X. Zhang, H. Fan, Journal of Materials Research 36 (13) (2021) 2639–2650.
[240] H. Su, Q. Zu, Z. Yang, H. Ye, International Journal of Plasticity 181 (2024) 104108.
[241] H. Somekawa, T. Tsuru, K. Naito, A. Singh, Scripta Materialia 249 (2024) 116173.
[242] G. Xi, J. Zhang, C. Fang, Materials Letters 182 (2016) 198–200.
[243] T. Tsuru, H. Somekawa, D.C. Chrzan, Acta Materialia 151 (2018) 78–86.
[244] Z. Li, H. Chen, Computational Materials Science 227 (2023) 112297.
[245] J. Wang, I.J. Beyerlein, Metallurgical and Materials Transactions A 43 (10) (2012) 3556–3569.
[246] J. Wang, I.J. Beyerlein, Modelling and Simulation in Materials Science and Engineering 20 (2) (2012) 024002.
[247] X. Liu, J. Wang, Scientific Reports 6 (1) (2016) 21393.
[248] C. Ni, H. Ding, M. Asta, X. Jin, Scripta Materialia 109 (2015) 94–99.
[249] Z. Xu, S. Tanaka, M. Kohyama, Modelling and Simulation in Materials Science and Engineering 29 (8) (2021) 085010.
[250] Z. Huang, V. Turlo, X. Wang, F. Chen, Q. Shen, L. Zhang, I.J. Beyerlein, T.J. Rupert, Computational Materials Science 188 (2021) 110241.
[251] H. Zhang, Y. Li, Z. Ding, T. Xie, R. Liu, Y. Li, D. Zhang, Q. Zhu, X. Shang, X. Zeng, Scripta Materialia 201 (2021) 113982.
[252] R. Pei, Z. Xie, S. Yi, S. Korte-Kerzel, J. Guénolé, T. Al-Samman, Scripta Materialia 230 (2023) 115432.
[253] P. Yang, H. Xie, S. Li, J. Zhu, X. Ma, J. Jin, H. Pan, Y. Ren, Y. Zong, W. Jia, et al., Acta Materialia 267 (2024) 119756.
[254] H. Xue, Y. Zhou, Z. Wei, M. Zhang, J. Li, Y. Liu, J. She, J. Hu, B. Jiang, Materials Research Letters 13 (10) (2025) 1001–1008.
[255] M. Wagih, P.M. Larsen, C.A. Schuh, Nature Communications 11 (1) (2020) 6376.
[256] J. Messina, R. Luo, K. Xu, G. Lu, H. Deng, M.A. Tschopp, F. Gao, Scripta Materialia 204 (2021) 114150.
[257] V. Menon, S. Das, V. Gavini, L. Qi, Acta Materialia 264 (2024) 119515.
[258] H. Zhang, Journal of Materials Research 24 (11) (2009) 3446–3453.
[259] H. Somekawa, T. Tsuru, Materials Science and Engineering: A 708 (2017) 267–273.
[260] H. Somekawa, T. Tsuru, A. Singh, Materials Science and Engineering: A 893 (2024) 146066.
[261] C.D. Barrett, A. Imandoust, A.L. Oppedal, K. Inal, M.A. Tschopp, H. El Kadiri, Acta Materialia 128 (2017) 270–283.
[262] C.D. Barrett, A. Imandoust, H. El Kadiri, Scripta Materialia 146 (2018) 46–50.
[263] M.K. Nahhas, S. Groh, Journal of Physics and Chemistry of Solids 113 (2018) 108–118.
[264] R. Mahjoub, M. Ferry, N. Stanford, Computational Materials Science 210 (2022) 111042.
[265] R. Mahjoub, D.A. Basha, A. Singh, M. Ferry, N. Stanford, Materials Science and Engineering: A 781 (2020) 139225.
[266] Z. Xing, H. Fan, G. Kang, Engineering Fracture Mechanics 275 (2022) 108866.
[267] M. Uranagase, R. Matsumoto, Computational Materials Science 118 (2016) 124–132.
[268] C. Xu, L. Yuan, R. Shivpuri, D. Shan, B. Guo, Modelling and Simulation in Materials Science and Engineering 27 (3) (2019) 035004.
[269] J. Ma, L. Yuan, Y. Duan, D. Shan, B. Guo, Journal of Materials Science 58 (38) (2023) 15219–15231.
[270] C. Xu, M. Zhang, X. Tian, W. Jiang, Q. Wang, H. Fan, Scripta Materialia 227 (2023) 115283.
[271] Y. Yue, J. Wang, J.-F. Nie, Journal of Magnesium and Alloys 11 (10) (2023) 3427–3462.
[272] S.-L. Hu, H.-H. Chen, Z. Zhang, Materials Today Communications 41 (2024) 110193.
[273] L. Liu, X. Luo, K. Papadikis, Y. Xin, Q. Liu, Journal of Magnesium and Alloys (2025).
[274] S. Zhou, P. Chen, X. Zhang, B. Li, H.-Y. Wang, Materials Research Letters 13 (4) (2025) 338–347.
[275] M. Liao, B. Li, M.F. Horstemeyer, Computational Materials Science 79 (2013) 534–539.
[276] M. Liao, B. Li, M.F. Horstemeyer, Metallurgical and Materials Transactions A 45 (8) (2014) 3661–3669.
[277] S. Groh, Materials Science and Engineering: A 618 (2014) 29–36.
[278] G. Esteban-Manzanares, A. Ma, I. Papadimitriou, E. Martínez, J. LLorca, Modelling and Simulation in Materials Science and Engineering 27 (7) (2019) 075003.
[279] G. Esteban-Manzanares, R. Alizadeh, I. Papadimitriou, D. Dickel, C.D. Barrett, J. LLorca, Materials Science and Engineering: A 788 (2020) 139555.
[280] R. Liu, L. Wang, M. Gong, X. Zeng, Journal of Magnesium and Alloys 13 (7) (2025) 3096–3103.

[281] Z. Huang, C. Yang, J.E. Allison, L. Qi, A. Misra, Journal of Alloys and Compounds 859 (2021) 157858.
[282] M.R. An, M.J. Su, R.N. Li, T. Ye, Q. Deng, H.Y. Song, C. Wang, Journal of Materials Research and Technology 27 (2023) 63–74.
[283] L. Han, H.Y. Song, M.R. An, T.Z. Shen, Y.L. Li, Journal of Non-Crystalline Solids 608 (2023) 122241.
[284] B. Li, S.N. Mathaudhu, Interaction between a Mg17Al12 precipitate and twin boundary in magnesium alloys, in: Magnesium Technology 2013, Springer, 2013, pp. 89–94.
[285] F.X. Wang, B. Li, Computational Materials Science 154 (2018) 472–480.
[286] H. Fan, Y. Zhu, Q. Wang, Computational Materials Science 155 (2018) 378–382.
[287] H. Fan, Y. Zhu, J.A. El-Awady, D. Raabe, International Journal of Plasticity 106 (2018) 186–202.
[288] H. Fan, J.A. El-Awady, Hardening effects of precipitates with different shapes on the twinning in magnesium alloys, in: Magnesium Technology 2019, Springer, 2019, pp. 257–261.
[289] J. Tang, W. Jiang, Q. Wang, X. Tian, D. Wei, H. Fan, Journal of Magnesium and Alloys 11 (2) (2023) 580–591.
[290] C. Xu, L. Yuan, H. Fan, Journal of Materials Engineering and Performance 33 (10) (2024) 4883–4897.
[291] W. Luo, C. Gasper, S. Zhang, P.L. Sun, N. Ulumuddin, A. Petrova, Y. Lysogorskiy, R. Drautz, Z. Xie, S. Korte-Kerzel, Acta Materialia 277 (2024) 120202.
[292] T. Stollenwerk, N.Z.Z. Ulumuddin, P.-L. Sun, S.-H. Lee, M. Seehaus, K. Skokov, O. Gutfleisch, Z. Xie, S. Korte-Kerzel, Acta Materialia 266 (2024) 119669.
[293] Z. Xie, D. Chauraud, A. Atila, E. Bitzek, S. Korte-Kerzel, J. Guénolé, Scripta Materialia 235 (2023) 115588.
[294] Z. Xie, D. Chauraud, A. Atila, E. Bitzek, S. Korte-Kerzel, J. Guénolé, Physical Review Materials 7 (5) (2023) 053605.
[295] A.F. Voter, F. Montalenti, T.C. Germann, Annual Review of Materials Research 32 (1) (2002) 321–346.
[296] A. Bochkarev, Y. Lysogorskiy, R. Drautz, Physical Review X 14 (2) (2024) 021036.